UNIVERSITAT POLITÈCNICA DE CATALUNYA
BARCELONATECH

UPCommons

Portal del coneixement obert de la UPC

http://upcommons.upc.edu/e-prints

Aquesta és una còpia de la versió *author's final draft* d'un article publicat a la revista *Chemical Engineering Journal.*

URL d'aquest document a UPCommons E-prints:

http://hdl.handle.net/2117/133392

Article publicat / Published paper:

Amani, A. [et al.]. Numerical study of binary droplets collision in the main collision regimes. (2019). *Chemical Engineering Journal*, vol. 370, p. 477-498. DOI: <10.1016/j.cej.2019.03.188>.

© <2019>. Aquesta versió està disponible sota la llicència CC-BY- NC-ND 4.0 http://creativecommons.org/licenses/by-nc-nd/4.0/

*Revised Manuscript (clean for typesetting)
Click here to view linked References

Numerical study of binary droplets collision in the main collision regimes

Ahmad Amani[a,*], Néstor Balcázar[b], Enrique Gutiérrez[a,b], Assensi Oliva[a,*]

[a] *Heat and Mass Transfer Technological Center (CTTC), Universitat Politécnica de Catalunya-Barcelona Tech((UPC), ESEIAAT, Colom 11, 08222 Terrassa (Barcelona), Spain*
[b] *Termo Fluids S.L. Avda Jacquard 97 1-E, 08222 Terrassa (Barcelona), Spain*
http://www.termofluids.com

Abstract

Direct numerical simulation of binary droplets collision is done using a conservative level-set method. The Navier-Stokes and level-set equations are solved using a finite-volume method on collocated grids. A novel lamella stabilization approach is introduced to numerically resolve the thin lamella film appeared during a broad range of collision regimes. This direction-independent method proves to be numerically efficient and accurate compared with experimental data. When the droplets collide, the fluid between them is pushed outward, leaving a thin gas layer bounded by the surface of two droplets. This layer progressively gets thinner and depending on the collision regime, may rupture resulting in coalescence of the droplets or may linger resulting in bouncing-off the droplets. Embedded ghost-nodes layer makes it possible to mimic both bouncing and coalescence phenomena of the droplets collision. The numerical tools introduced are validated and verified against different experimental results for a wide range of collision regimes. A very good agreement is observed between the results of this paper and experimental data available in the literature. A detailed study of the energy budget for different shares of kinetic and dissipation energies inside of the droplet and matrix, in addition to the surface tension energy for studied cases, is provided. Supplementary quantitative values of viscous dissipation rate inside of the matrix and droplet, and also the radial expansion of the droplet are presented as well.

Keywords: Comprehensive droplets collision regimes, Conservative Level-set, Lamella stabilization, Energy analysis

*Corresponding author
Email addresses: ahmad@cttc.upc.edu.com (Ahmad Amani), nestor@cttc.upc.edu (Néstor Balcázar), kike@cttc.upc.edu (Enrique Gutiérrez), oliva@cttc.upc.edu (Assensi Oliva)

1. Introduction

The dynamics of binary droplets collision is of huge importance in different fields, from multiphase reactors [1], raindrop formation [2], ink-jet printing, spray combustion, emulsion stability, turbine blade cooling, spray coating [3, 4], to drug delivery, e.g. by encapsulating one liquid within another one used in the context of drugs in lungs [5]. Due to the complexity of the nature of droplets collision, this topic is one of the most challenging areas in the field of fluid dynamics. The outcome of the droplets collision can profoundly affect the overall performance of many systems. For example in fuel sprays near the injector in internal combustion engines or gelled hypergolic propellants in rocket engines, the outcome of the collisions, the size distribution, dissipated energy of the droplets and number of satellite droplets can affect the overall combustion efficiency. Binary droplets collision as two droplets collide each other are the most common interaction in aerosol sprays where ternary and more complex collisions are rare. Droplets collision has been the topic of numerous investigations, including experimental, analytical and numerical studies.

Experimental studies are providing us with different correlations to understand the droplets collision. The main parameters are the surface tension coefficient σ, droplet viscosity μ_d, droplet density ρ_d, droplets relative velocity U_{rel}, and the impact parameter I. The following non-dimensional parameters are thus defined by most researchers to characterize the droplets collision:

$$We = \frac{\rho_d {U_{rel}}^2 D_0}{\sigma}, \quad Re = \frac{\rho_d U_{rel} D_0}{\mu_d}, \quad Oh = \frac{\mu_d}{\sqrt{\rho_d \sigma D_0}}, \quad I = \frac{b}{D_0} \tag{1}$$

where We is the Weber number presenting the ratio between inertial forces and surface tension, Re is the Reynolds number representing the ratio of the inertial and viscous forces, and Oh is the Ohnesorge number representing the ratio of viscous forces and the combined effect of inertial forces and surface tension. In this formulation D_0 is the droplet's initial diameter and subscript **d** is the abbreviation of the word *droplet*. The impact parameter I characterizes the eccentricity of the collision with b as the inter-center distance of the droplets in direction normal to the collision.

Experimental research started with the works of Brazier-Smith et al. [6] where they studied the interaction of falling water droplets. Brenn and Frohn [7] investigated the collision and coalescence of droplets of different liquids. Ashgriz and Poo [3] studied the binary collision of two water droplets of equal and unequal sizes. They concluded that the collision dynamics could be characterized based on the droplets size ratio, collision Weber number and the impact parameter (I) where the Weber number presents the ratio between inertial forces and surface tension and impact parameter characterizes the eccentricity of the droplets in the collision

direction. Qian and Law [4] presented a detailed description of collision dynamics based on a series of time-resolved images of the collisions for different regimes of head-on and off-center. They provided a map based on Weber number and Impact parameter separating collision regimes in a We-I nomograph as shown in figure 1. They concluded the existence of five regimes as:

1. SPC (soft permanent-coalescence): coalescence after minor deformation.
2. B: Bouncing of the droplets.
3. HPC (hard permanent-coalescence): Coalescence after substantial deformation
4. CFRS (coalescence followed by reflexive separation): Coalescence followed by separation for near head-on collisions.
5. CFSS (coalescence followed by stretching separation): Coalescence followed by separation for off-center collisions.

Jiang et al. [8] investigated the collisional dynamics of equal-sized water and normal-alkane droplets. Willis and Orme [9] conducted experimental research on binary droplet collisions in a vacuum environment to study the dynamics of the collision in the absence of aerodynamic effects. Pan et al. [10] experimentally and numerically investigated the dynamics of head-on droplets collision. Utilizing the empirically supplied information in the numerical simulations, they further studied different parameters of the collision including the thickness of the gap gas and flow properties around the interface. Tang et al. [11] studied collision of unequal-sized droplets in different regimes. They provided a unified regime diagram concerning bouncing, coalescence, and separation for hydrocarbon and water droplets. On a more advanced work, Pan et al. [12] used a technique developed for generating high-speed droplets to investigate binary droplets collision at Weber numbers up to 5100. Planchette et al. [13] experimentally examined the onset of fragmentation in head-on binary and ternary droplets collisions. With the help of extracted data, they provided a general model for predicting the velocity threshold in fragmentation of collisions. Pan et al. [14] investigated the effect of surfactants on controlling the droplets bouncing and coalescence. Estrade et al. [15] studied the binary droplet collision of ethanol droplets. They also proposed a theoretical model to predict the droplet coalescence and bouncing outcome.

Analytical studies in this field are performed to a great extent to predict the outcome of a particular type of collision. Reitz and D. [16] presented a simplified model of droplet-shattering collision. Gopinath [17] analyzed the head-on collision and subsequent rebound of two droplets for small Weber numbers. Bach

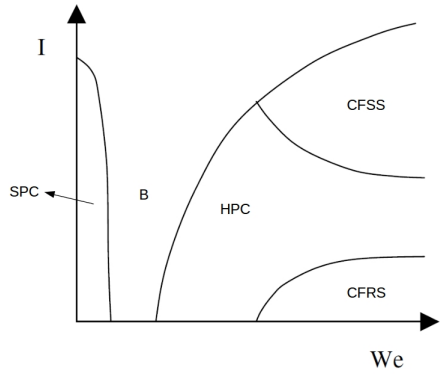

Figure 1: We-I diagram for collision outcome regimes as reported by Qian and Law [4].

et al. [18] presented a theory based on potential flow in the liquid, weak deformation of the gas-liquid interfaces, and non-continuum viscous flow in the lubrication gas film for minimal Weber numbers. Zhang and Law [19] suggested a unified theoretical description of head-on equal-sized droplets. They have made important advances in presenting a general formulation for a wide range of Weber numbers. In a more recent research, Li [20] predicted the coalescence-bouncing transition of head-on binary droplets collision using a macroscopic model. He has modified the Navier-Stokes equations to account for the inter-droplet gas film using the lubrication theory of Zhang and Law [19].

The flexibility of numerical simulations on implementing different initial conditions, boundary conditions and fluid properties, as well as their capability to extract substantial information on the flow field, makes them extra appealing on studying multiphase flow problems. Numerical simulations of droplets collision can provide significant details on the nature of the collision, e.g. energy analysis of the droplets, air gap thickness, velocity and vorticity fields which are difficult or impossible to capture experimentally or analytically. As a result, significant attention was given to numerical simulations of droplets collision.

The volume-of-fluid (VOF) method along with an adaptive mesh refinement methodology was employed by Nikolopoulos and Bergeles [21] to study the binary droplets collision for cases with Weber numbers up to 61.4. Good agreement was achieved between their simulations and the experimental results. In another work, Nikolopoulos et al. [22] studied the off-center binary droplets collision using an adaptive mesh refinement technique. However, a stable lamella film was not captured for high Weber numbers. Chen et al. [23] studied the droplets collision dynamic using an improved VOF technique, an adaptive mesh refinement algorithm

and mass transfer process. Although the VOF method conserves the mass property of the droplets, it suffers the accuracy for calculation of normal and curvature of the interfaces.

In the category of the level-set method, Pan and Suga [24] used a level-set/finite-volume method to simulate three-dimensional collisions for a wide range of Weber numbers. Uniform mesh with small grid sizes was used in their work ($D_0/60$-$D_0/80$ with D_0 as the initial diameter of the droplets). Good agreement was seen in their results compared with experimental snapshots. Tanguy and Berlemont [25] applied a level-set/finite-difference approach on the collision of droplets for cases with Weber numbers up to 83. A disadvantage of the level-set method is that the discrete solution of transport equations is inclined to numerical error which results in loss or gain of mass in the droplets. Kwakkel et al. [26] developed a coupled level-set/volume-of-fluid (CLSVOF) method for droplet-laden flows to accommodate coalescence and breakup of the droplets. They have mentioned that the film drainage time calculated by the model of Zhang and Law [19] is not sufficiently accurate to capture the correct physics of the collision. Recently, Balcázar et al. [27] used a novel multiple-marker approach for simulating the bouncing of the droplets, in the framework of a conservative level-set method, which circumvents the mass conservation issue.

In the category of the front-tracking method, Nobari et al. [28] conducted two-dimensional axisymmetric simulation of head-on collision process using a front-tracking/finite-difference method in low density-ratio flows. Later on, Pan et al. [10] used the three-dimensional version of this method to simulate cases with Weber numbers up to 13. Zhang and Zhanga [29] studied the kinetic energy recovery and the interface hysteresis of bouncing droplets. In the Front-tracking method, a fixed Eulerian grid is used for the fluid flow, and a separate Lagrangian grid is used to track the interface explicitly. Despite the accuracy of this method, it is complicated to implement (due to dynamic re-meshing of the Lagrangian interface mesh), and also difficulties arise when multiple interfaces interact with each other.

In the category of lattice Boltzmann method, Lycett-Brown et al. [30] performed a three-dimensional binary droplets collision research using a multiphase cascaded lattice Boltzmann method for Weber numbers as high as 100. Moqaddam et al. [31] used an entropic lattice Boltzmann method to simulate high Weber number collision cases with lamella films. Premnath and Abraham [32] Used a multi-relaxation-time multiphase flow lattice Boltzmann model to solve head-on and off-center binary droplets collision. In another work Dupuy et al. [33] simulated high-pressure binary droplets collision. Baroudi et al. [34] examined the effect of initial conditions on the simulation of inertial coalescence of two droplets. Sun et al. [35] numerically investigated the head-on unequal-sized collision of droplets using a multiple-relaxation-time lattice Boltzmann model. Mazloomi et al. [36] presented a novel thermodynamically consistent lattice Boltzmann

model enable to control the dynamics at the liquid-vapor interface. Lycett-Brown and Luo [37] Used a cascaded lattice Boltzmann to simulate large density ratio binary droplet collisions. Monaco et al. [38] studied the collision of two microdroplets with a pseudopotential multiple-relaxation-time lattice Boltzmann model. Besides the macro scales, there are researches studying the droplets collision phenomena in molecular scales [39].

Despite all the advances in the numerical simulation of droplets collision, this area is still a challenging topic regarding the difficulties related to the tracking of interfaces, mass conservation of the droplets, numerical disintegration of the lamella film, instabilities encountered by large density ratio and surface tensions. In this paper, we study the binary head-on and off-center collision of equal-sized droplets for all the collision regimes as initially discussed by Qian and Law [4]. We introduce a novel and computationally-efficient lamella stabilization approach to resolve the thin lamella film formed during a wide range of collision regimes. We perform the energy analysis of all the cases studied, and provide qualitative graphs to benchmark these cases for future validation purposes. Furthermore, to the best of the authors' knowledge, there are no previous studies of binary droplet collision using a conservative level-set (CLS) method. Therefore, as an additional novelty, this research is performed in the framework of a CLS method introduced in Balcazar et al. [40] for interface capturing on unstructured meshes. In the present CLS method, interface normals are computed using a least-squares method on a wide and symmetric nodes-stencil around the vertexes of the current cell. These normals are then used for an accurate computation of surface tension, without additional reconstruction of the distance function, as in geometrical volume-of-fluid/level-set methods [41] or fast-marching methods. Moreover, most computational operations are local, indeed this method has been efficiently implemented on parallel platforms [40, 42]. Furthermore, unstructured flux-limiter schemes introduced in [40] are used to advect the CLS function and momentum, avoiding numerical oscillations at discontinuities, and minimizing the numerical diffusion. Finally, the present finite-volume formulation is attractive due to its simplicity and the satisfaction of the integral forms of the conservation laws over the entire domain.

The rest of the paper is organized as follows: mathematical formulations are presented in section 2, numerical discretization of governing equations are described in section 3.1. Gas-film and lamella stabilization algorithms are explained in section 3.3 and 3.4, respectively. Results and discussions are reported in section 4 and at the end, conclusion remarks are provided in section 5.

2. Mathematical formulation

Navier-Stokes equations are used to describe the conservation of mass and momentum of two incompressible immiscible Newtonian fluids on a spacial domain Ω with boundary $\partial\Omega$ as following [40]:

$$\frac{\partial}{\partial t}(\rho\mathbf{v}) + \nabla\cdot(\rho\mathbf{v}\mathbf{v}) = \nabla\cdot\mathbf{S} + \rho\mathbf{g} + \sigma\kappa\mathbf{n}\delta_\Gamma \text{ in } \Omega \tag{2}$$

$$\mathbf{S} = -p\mathbf{I} + \mu(\nabla\mathbf{v} + (\nabla\mathbf{v})^T) \tag{3}$$

$$\nabla\cdot\mathbf{v} = 0 \text{ in } \Omega \tag{4}$$

where ρ and μ are density and dynamic viscosity of the fluids, $\mathbf{v}$ is the velocity field, $\mathbf{S}$ is the stress tensor, p pressure field, $\mathbf{g}$ gravitational acceleration and δ_Γ is the Dirac delta function concentrated at the interface (Γ). In this formulation, $\mathbf{n}$ is the normal unit vector outward to interface, κ is the interface curvature, and σ is the interface tension coefficient.

Taking into account that mass, density and viscosity are constant within each fluid, they can be defined as scalar-fields inside the whole domain as follows:

$$\rho = \rho_1 H + \rho_2(1-H) \tag{5}$$

$$\mu = \mu_1 H + \mu_2(1-H) \tag{6}$$

where H is the Heaviside step function taking the value one in dispersed phase and zero elsewhere. In this research, conservative level-set (CLS) method as introduced by Balcázar et al. [40] in the context of a finite-volume method and unstructured meshes is used. Instead of the signed distance function, d(x,t), used to represent the interface in the classical level-set method, conservative LS method employs a regularized indicator function ϕ as below:

$$\phi(x,t) = \frac{1}{2}\left(tanh\left(\frac{d(x,t)}{2\varepsilon}\right) + 1\right) \tag{7}$$

where ε is the parameter that sets the thickness of the interface. ϕ varies from 0 in one fluid to 1 in other fluid. With this formulation, interface is defined by $\mathit{\Gamma} = \{x|\phi(x,t) = 0.5\}$.

The level-set function is advected by velocity vector field, $\mathbf{v}$, obtained from solution of Navier-Stokes equations. Taking into account the incompressibility constraint (equation 4), the interface transport equation

can be transformed to the conservative form [40, 43] as:

$$\frac{\partial \phi}{\partial t} + \nabla \cdot \phi \mathbf{v} = 0 \tag{8}$$

Since sharp changes exist in level-set function at the interface, flux-limiter schemes are required to discretise the convective term to minimise numerical diffusion and avoid numerical instabilities at the interface. An additional re-initialization equation is used to keep the profile and thickness of the interface constant:

$$\frac{\partial \phi}{\partial \tau} + \nabla \cdot \phi \left(1 - \phi\right) \mathbf{n}_{\tau=0} = \nabla \cdot \varepsilon \nabla \phi \tag{9}$$

This equation which is advanced in pseudo-time τ, consists of a compressive flux $(\phi(1-\phi)\mathbf{n}_{\tau=0})$ which keeps the level-set function compressed onto the interface along the normal vector $\mathbf{n}$, and a diffusion term $(\nabla \cdot \varepsilon \nabla \phi)$ which keeps the profile in prescribed characteristic thickness of ε. This parameter is defined based on the mesh resolution as [40, 43]:

$$\epsilon_p = C_\epsilon h^{1-\alpha} \tag{10}$$

where $h = (Vol_P)^{1/3}$ is the grid size, with Vol as the volume of the computational cell. Generally, the value of α can vary between [0,0.1], to overcome the possible numerical instabilities, but in all of our simulations, α value was chosen equal to 0.0. The value of C_ϵ is equal to 0.5. Normal vector $\mathbf{n}$ and curvature κ of the interface, are obtained using [40]:

$$\mathbf{n} = \frac{\nabla \phi}{||\nabla \phi||} \tag{11}$$

$$\kappa(\phi) = -\nabla \cdot \mathbf{n} \tag{12}$$

The continuous surface force model (CSF) [44] is used for surface tension computation which converts the term $\sigma \kappa \mathbf{n} \delta_\Gamma$ in Eq. 2 to a volume force term of $\sigma \kappa(\phi) \nabla \phi$ [40]. Where $\nabla \phi$ is computed using least-square method based on vertex node stencils [40]. By applying this approach, the explicit tracking of the interface is not necessary.

3. Numerical method

3.1. Discretization of governing equations

Finite-volume (FV) approach is used to discretise the Navier-Stokes and level-set equations on a collocated grid meaning all the computed variables are stored at centroids of the cells [40]. A central difference (CD) scheme is used to discretise the compressive term of re-initialization equation (9) and diffusive fluxes at the faces. A distance-weighted linear interpolation is used to calculate the face values of physical properties and interface normals. The gradients are computed at the cell centroids by a least-squares method using a stencil that includes the cell-nodes around the vertexes of the current cell [40].

As in this paper, we are analysing the energy budget of the collisions, the choice of flux-limiter in the discretization of convective terms of momentum and advection equations must be accordingly, to obtain the highest accuracy in total energy conservation of the system. Appendix A provides a detailed study on the effect of different flux-limiters on total energy conservation of a two-phase system and the spatial convergence rate of the chosen one. According to these results, unless otherwise is mentioned, a total-variation Diminishing (TVD) flux-limiter of Superbee is used in all the simulations of this paper.

At discretized level, physical properties are regularized in the context of the CLS method. Therefore a linear average is used for density as $\rho = \rho_1\phi + \rho_2(1-\phi)$, and viscosity as $\mu = \mu_1\phi + \mu_2(1-\phi)$.

A classical fractional step projection method as described by Chorin [45] is used to solve the velocity-pressure coupling. The solution procedure is as follows:

1. Physical properties, interface geometric properties and velocity field are initialized.

2. Maximum allowable time step is calculated using the CFL conditions on the convective and diffusive terms of momentum equation and also by explicit treatment of surface tension as used by Balcazar et al. [40]:

$$\Delta t \equiv \alpha \times min\left(\frac{h}{\|V_P\|}, \frac{h^2\rho(\phi_P)}{\mu(\phi_P)}, h^{3/2}(\frac{\rho_1+\rho_2}{4\pi\sigma})^{1/2}\right) \tag{13, 14}$$

   where α as the CFL coefficient in this study is equal to 0.1.

3. The advection equation (8) is integrated in time with a 3-step third order accurate TVD Runge-Kutta scheme [46].

4. The re-initialization equation (9) is integrated in pseudo time (τ) using a third order accurate TVD Runge-Kutta scheme. Time τ is used to lead the solution into a stationary state. Since an explicit scheme is used, the time step is restricted by the viscous term of equation 9 as $\Delta\tau = C_\tau min\left(h^2/\epsilon_P\right)$ [40, 43]. One iteration is used to solve the discretized form of equation 9. The value of C_τ serving as a CFL-like coefficient for this equation is equal to 0.05.

5. Physical properties in the domain (density and viscosity) and geometrical properties at the interface (curvature and interface normal) are updated from the level-set field.

6. The velocity and pressure fields are calculated using a classical fractional-step method first introduced by Chorin [45]. The first step is to calculate the predicted velocity $\mathbf{v}$. A second-order Adam-Bashforth scheme is used for the temporal discretization of convective, diffusive and surface tension terms.

$$\frac{\rho\mathbf{v}^* - \rho^n\mathbf{v}^n}{\Delta t} = \frac{3}{2}(R_h^v)^n - \frac{1}{2}(R_h^v)^{n-1} \tag{15}$$

where $R_h^v = -\mathbf{C}_h(\rho\mathbf{v}) + \mathbf{D}_h(\mathbf{v}) + \sigma\kappa\nabla_h(\phi)$ with $\mathbf{C}_h(\rho\mathbf{v}) = \nabla_h \cdot (\rho\mathbf{v}\mathbf{v})$ as the convective operator, $\mathbf{D}_h(\mathbf{v}) = \nabla_h \cdot \left(\mu(\nabla_h\mathbf{v} + \nabla_h^T\mathbf{v})\right)$ as the diffusive operator and ∇_h as the gradient operator.

A correction to the predicted velocity applies as:

$$\frac{\rho\mathbf{v}^{n+1} - \rho\mathbf{v}^*}{\Delta t} = -\nabla_h\mathbf{P}^{n+1} \tag{16}$$

By applying the incompressibility constraint ($\nabla \cdot \mathbf{v} = 0$), equation 16 changes to a Poisson equation as follows:

$$\nabla_h \cdot \left(\frac{1}{\rho}\nabla_h(\mathbf{P}^{n+1})\right) = \frac{1}{\Delta t}\nabla_h \cdot (\mathbf{v}^*) \tag{17}$$

The obtained linear system is solved using a preconditioned conjugated gradient method. At the end, the velocity $\mathbf{v}^{n+1}$ is corrected using:

$$\mathbf{v}^{n+1} = \mathbf{v}^* - \frac{\Delta t}{\rho}\nabla_h(\mathbf{P}^{n+1}) \tag{18}$$

7. To fulfill the incompressibility constraint (equation 4) and to avoid pressure-velocity decoupling on collocated meshes [47], a cell-face velocity is used to advect the momentum and CLS function, as introduced in [40, 48].

8. repeat steps 2 -7 to reach the desired time.

The reader is referred to [48, 40] for technical details on the finite-volume discretization of both the Navier-Stokes and conservative level-set equations on collocated unstructured grids. The numerical methods are implemented in an in-house parallel c++/MPI code called TermoFluids [49]. Validations and verifications of the numerical methods in the context of Conservative level-set method used in this work have been reported in [40, 50, 51, 52, 53, 48, 54, 55].

3.2. Energy analysis of the system

For all the cases solved in this study, we have monitored the energy budget throughout the collision process. Taking into account the energy conservation law, we expect that the total energy (**TE**) of the system must be constant during the collision, and be equal to its initial value, i.e. the summation of the initial Kinetic energy ($\mathbf{KE}_{init}$) and the initial Surface tension energy ($\mathbf{STE}_{init}$). This value must be equal to the summation of kinetic, surface tension and total dissipated energies (**TDE**) in each given time t.

$$\mathbf{TE} = \mathbf{KE}_{init} + \mathbf{STE}_{init} = \mathbf{KE}(t) + \mathbf{STE}(t) + \mathbf{TDE}(t) \tag{19}$$

Kinetic energy [J] at a give time is calculated by summation of spacial integration of $\frac{1}{2}\rho V^2$ over all the cells with V as the second norm of the velocity vector in an arbitrary cell P as:

$$\mathbf{KE}(t) = \sum_{cells} \left(\int_p \frac{1}{2} \rho V^2 dv_p \right) \tag{20}$$

Surface tension energy [J] is calculated as $\sigma\mathbf{S}(t)$ where $\mathbf{S}$(t) is the surface area of the interface. The value of $\mathbf{S}$(t) is equal to:

$$\mathbf{S}(t) = \sum_{cells} \left(\int_p ||\nabla\phi|| dv_p \right) \tag{21}$$

TDE(t) [J] is calculated by temporal integration of viscous dissipation rate (**VDR**(t)) from the beginning

of the simulation until time t:

$$\mathbf{TDE}(t) = \int_0^t \mathbf{VDR}(t)dt \tag{22}$$

VDR(t) [J/s] is obtained by summation of spatial integration of viscous dissipation function (**VDF**(t)) over all the cells:

$$\mathbf{VDR}(t) = \sum_{cells} \left(\int_p \mathbf{VDF}(t)dv_p \right) \tag{23}$$

In this formulation, the value of **VDF** [J/(s.m^3)] quantifies the local volumetric viscous dissipation rate in each cell and is calculated by:

$$\mathbf{VDF} = \mu \left(\nabla V + \nabla V^T \right) : \nabla V \tag{24}$$

The share of **KE** and **TDE** budgets could be divided into two subdomains of droplet and matrix using the introduced level-set function (ϕ), e.g.:

$$\mathbf{KE}_{drop} = \mathbf{KE} \times \phi \tag{25}$$

$$\mathbf{KE}_{matrix} = \mathbf{KE} \times (1 - \phi) \tag{26}$$

A three-dimensional droplet deformation test case is used to verify the accuracy of our formulations in calculating the energy budgets of the simulations. The details of this study is provided in supplementary material, section 1.

3.3. Gas-film stabilization approach

During the collision process, a thin gas film is formed between the droplets. The consistency of this gas film results in bouncing and rupture of it results in coalescence of the droplets. The thickness of this gas film is in the order of nanometers and CFD simulation of it is almost impossible. Different approaches have been tried by researchers to tackle this problem. Mason et al. [56] presented a subgrid-scale model to account for the gas film drainage due to the computational difficulty of capturing all the length scales involved with a single discretized mesh. Jiang and James [57] developed numerical models to incorporate the van-der-Waals forces in the Navier-Stokes equations with the assumption that the interface slope is small. They used

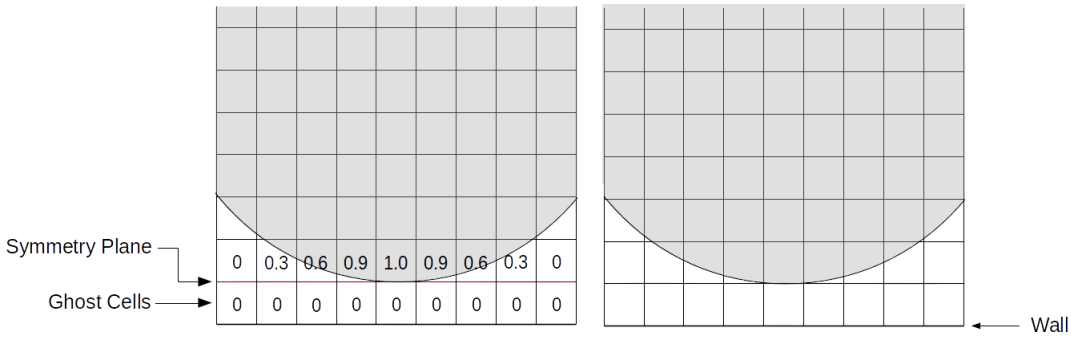

Figure 2: (left) Illustration of the implemented ghost-nodes and symmetry plane used to imitate the gas rupture persistence. (right) removal of ghost-nodes layer for the times after gas film rupture.

two methods, one by introducing the van-der-Walls forces as a body force in the momentum equation and other by employing the van-der-Waals forces in terms of a disjoining pressure in the film depending on its thickness. Li [20] employed a macroscopic model for head-on binary droplets collision by solving a length scale range of five orders of magnitude.

According to the experimental results and analysis of Qian and Law [4], before coalescence, due to the existence of gas film between the droplets, the topology evolution of collision is similar to the bouncing of two droplets. The time when the thickness of inter-droplets gas film reaches a minimum value is noted as the critical time in topology evolution of the droplets collision. At this critical time, the droplets lack enough kinetic energy to squeeze the gas film further. The future of the collision depends on whether the gas film rupture will happen or not. Therefore, this critical time can also be assigned as the gas film rupture time. For collisions with relatively high Weber number it is assumed that the gas film rupture time is belittle and there is no need for special numerical treatment of it [26]. For collisions with relatively lower Weber number including SPC, B and some cases in HPC regime, however, the gas film rupture time has substantial effect on the collision outcome. As a result, the HPC regime can be sub-categorized into:

- Retarded permanent coalescence, when the gas film rupture time is considerable
- Immediate permanent coalescence, when the gas film rupture time is negligible

In this study we have used ghost-nodes method to control the gas film rupture for cases of regimes *SPC*, *B* and *retarded HPC* . For these cases, instead of collision of two droplets, the collision of a droplet with a symmetry wall with ghost-nodes is studied. Figure 2 illustrates the concept of ghost-nodes layer in determining the droplets collision outcome. Implementing the Dirichlet boundary condition for level-set

function in these nodes imitates the persistence of gas film and thus bouncing of droplets. In the previous works in literature, the researchers were using the Neumann boundary condition in the ghost-nodes to imitate the rupture of the gas film, resulting in coalescence of the droplets. We believe this injects mass into the system and is not advised since it does not conserve the mass of the droplet. In this work, instead of using Neumann boundary condition on ghost-nodes layer to imitate the gas rupture, we merely remove the ghost-nodes layer, allowing the droplet to approach the wall with symmetry boundary condition applied to it.

Removing the ghost-nodes layer in a prescribed time enables us to model the retarded coalescence phenomena (SPC and retarded HPC regimes). Considering the above explanations, to simulate the retarded coalescence cases, one needs the time for rupture of the gas film. To do so, we first simulate a bouncing collision of a droplet with the ghost-nodes layer and monitor the thickness of the gas film during the collision process. The time where the gas film reaches its minimum value will be counted as the rupture time. We then restart the simulation and apply the calculated rupture time as the time when we remove the ghost-nodes layer from the simulation, e.g. change the collision regime from bouncing to coalescence. Thus, three steps are taken into account to simulate a head-on retarded coalescence of colliding droplets:

- Applying ghost-nodes layer boundary condition in the collision direction to monitor the thickness of the gas film during the collision process.
- Calculating the time related to minimum gas film thickness.
- Prescribing the calculated time as the time when the ghost-nodes layer is begin removed from the simulation. (e.g. switching from bouncing regime into coalescence regime).

3.4. Lamella Stabilization Approach

The collision of two droplets at an enough high Weber number results in the formation of an extremely thin film called lamella. As reported in [58, 3, 4], the rupture of a lamella film is not observed in droplets collision for Weber numbers as high as 2800 indicating that lamella rupture which happens in numerical simulations is a numerical artifact and needs to be prevented in order to capture the correct physics of the collision. The numerical rupture of lamella film results in deflection of the shape and physics of the collision complex [22]. Figure 3 illustrates exemplarily the shape of the collision outcome for two cases, one with lamella resolved and other with standard simulation.

The thickness of lamella film is of smallest scales of the simulations and numerical resolution of it implies

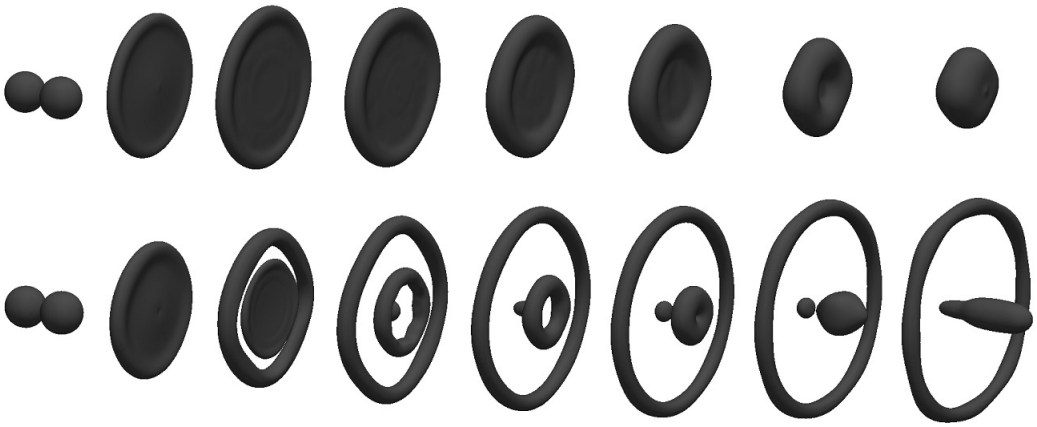

Figure 3: Droplets collision outcome for two cases of binary head-on collision with We=269 and Re=154. Stabilized lamella (first row) and standard simulation (second row). Both simulations are performed in a domain with a fine grid size of h=D/50.

enormous extra computational cost through the usage of extremely fine meshes or adaptive-mesh-refinement techniques. Its numerical resolution in case of collisions with very high Weber numbers is almost impossible.

According to [59, 60], the primary cause of numerical lamella rupture is due to the interaction in the computation of surface tension forces of its both sides and also incorrect surface reconstruction caused by artificial interface interaction. Focke and Bothe [59] and Liu and Bothe [60] suggested that both of these problems could be prevented by identifying the lamella film and afterwards treating the cells of the opposite sides of the lamella as they called it "fully wetted". They proceeded the solution by injecting mass into the lamella layer to keep its thickness more than one grid cell. In the algorithm of [59], it is necessary to calculate the angle between X direction and the lamella, immediately before its rupture, and then restart the simulation with the rotated domain so that lamella is perpendicular to the X direction. Proposed algorithm of [60] however can be used only for the head-on collision of the droplets where the collision solution could be replaced by the collision of one droplet with a ghost-nodes layer. In this section, we introduce a novel approach towards the stabilization of the lamella film which overcomes the aforementioned problems.

In the presented conservative level-set method, the interface profile is resolved in a smooth transition of ϕ at the interface. The width of the transition region depends on the diffusion coefficient ϵ defined in equation 10. Figure 4 presents the interface of an arbitrary collision of droplets in the matrix fluid, resolved by structured square grids along with the transition of the level-set function ϕ from 1 inside of the droplet to 0 in the matrix fluid for the direction $\mathbf{n}$ normal to the interface. Figure 5(a) presents the interface of the same collision as figure 4, advanced in time where the lamella film appears in the collision complex. Figure

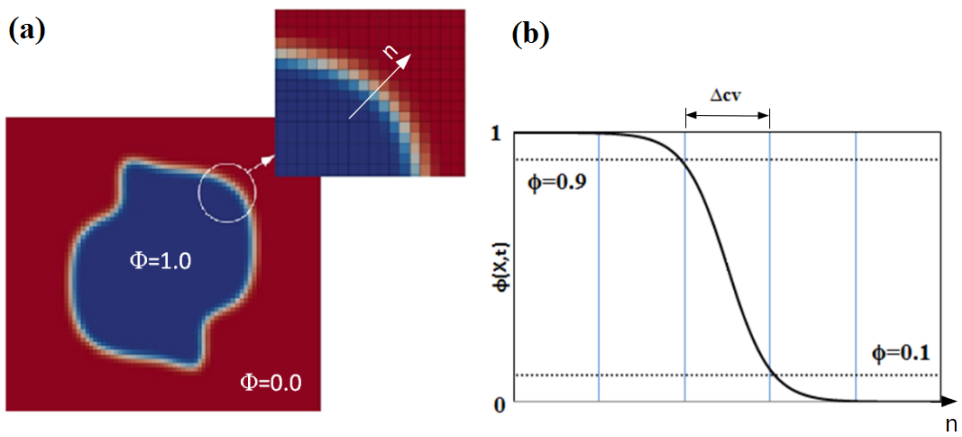

Figure 4: (a): Interface of an arbitrary collision of droplets in a matrix fluid along with (b): transition of the level-set function ϕ from 1 inside of the droplet to 0 in the matrix for the direction $\mathbf{n}$ normal to the interface.(Δ_{cv} is the grid size of the cell cv)

5(b) illustrates the transition of the level-set function (ϕ) for the direction $\mathbf{n}$ normal to the interface from 0 in the matrix fluid, to 1 inside of the droplet and again to 0 in the matrix fluid. In this figure, $\boldsymbol{\ell}_2$ is the interface thickness in the lamella film and $\boldsymbol{\ell}_1$ is the length of the portion of lamella which contains only pure droplet material.

We define the physical center of the lamella film in $\mathbf{n}$ direction as cell $\mathbf{P}$ which exhibits a behavior like figure 5(b). In a simulation, there might be many cells satisfying this condition. If $\boldsymbol{\ell}_1 > \Delta_P$ (with Δ as the characteristic length of the cell in $\mathbf{n}$ direction), no special treatment of lamella is required. The numerical artifact of lamella starts when the value of this parameter decreases to $\boldsymbol{\ell}_1 \leq \Delta_P$. In the moment in which $\boldsymbol{\ell}_1 = \Delta_P$, supposing the neighboring cells of $\mathbf{P}$ in direction normal to the interface are F_1 and F_2, then the values of ϕ_{F_1} and ϕ_{F_2} will be smaller than $\phi_P = 1.0$. Keeping in mind the calculation of the $\nabla\phi$ described in section 3.1, at this moment, the value of $(\nabla\phi)_P$ will decrease dramatically, resulting in decreasing the value of $(\sigma\kappa(\phi)\nabla\phi)_P$ in momentum equation. Decreasing the value of surface tension at this point will accelerate the decay of its level-set function value which leads to the rupture of the lamella film. In order to prevent this, we propose to follow the lamella changes, considering the moment of $\boldsymbol{\ell}_1 = \Delta_P$ as a milestone (herein after refereed to as *critical stage*). When the value of ϕ_P falls bellow 1.0, we add $\zeta = (1.0 - \phi_P)$ to ϕ_P to keep its value at critical stage of $\phi_P = 1.0$. The important question now is how to detect the points like $\mathbf{P}$ as the centers of the lamella film in $\mathbf{n}$ direction. We believe that if $\mathbf{P}$ point has the level-set characteristics as figure 5(b) in $\vec{\mathbf{n}}$ direction, it will also has similar behavior in at least one of the $\mathbf{X}$, $\mathbf{Y}$ or $\mathbf{Z}$ directions. Thus,

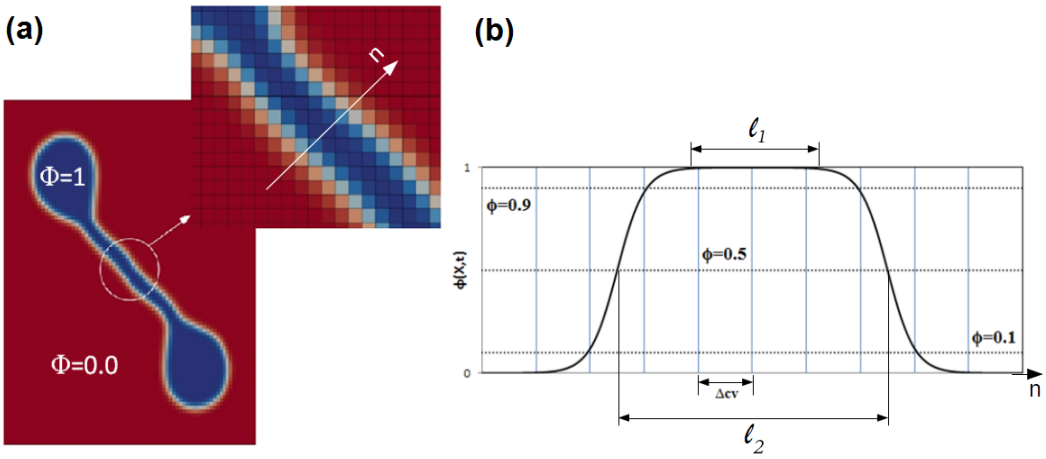

Figure 5: (a): The interface of the same collision as figure 4, advanced in time where the lamella film appears in the collision complex. (b): transition of the level-set function (ϕ) for the direction **n** normal to the lamella film from 0 in the matrix fluid, to 1 inside of the droplet and again to 0 in the matrix fluid. ($\boldsymbol{\ell}_2$ is the interface thickness in the lamella film and $\boldsymbol{\ell}_1$ is the length of the portion of lamella which contains only pure droplet material)

in order to simplify the solution procedure, we look for **P** points where they demonstrate the hunchback variation of ϕ not in $\vec{\mathbf{n}}$ direction but in at least one of the **X**, **Y** or **Z** directions, depending on which direction $\vec{\mathbf{n}}$ is more leaned towards. To do so, we propose the following steps for every point in the interface, within the solution algorithm:

1. Determine the direction of the checking (**X**, **Y** or **Z**): it is possible to use the value of $\vec{\mathbf{n}}$ vector at the cell location ($\vec{\mathbf{n}} = (n_x, n_y, n_z)$). The direction associated with the maximum absolute value of the components of $\vec{\mathbf{n}}$ will be assigned as the checking direction. E.g. if $|n_x| > |n_y| > |n_z|$, the checking direction will be **X**.

2. Find the neighboring points of the cell of interest in the calculated checking direction, (F_1 and F_2).

3. Check if the cell exhibits hunchback variation of ϕ at critical stage (e.g. if $\phi_P > \phi_{F_1}$ and $\phi_P > \phi_{F_2}$). If so, add the value of $\zeta = (1.0 - \phi_P)$ to ϕ_P.

The solution algorithm for the proposed lamella stabilization method is explained in algorithm 1. With special care, the whole solution procedure can be written without any **if** conditions, as we did, to impose the minimum possible computational cost. The algorithm to check and stabilize lamella can be started from the beginning of the simulations. Once the number of modified **P** cells from a non-zero value returns to zero, it

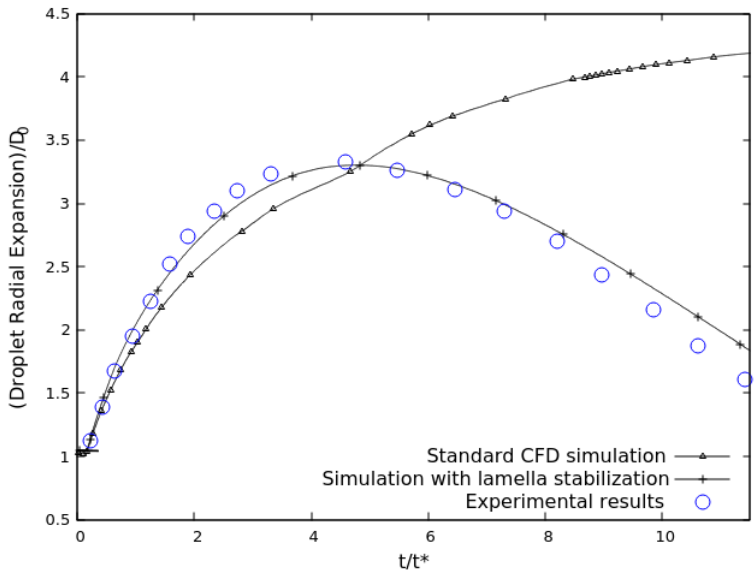

Figure 6: Radial expansion of the head-on collision complex of two droplets with We=269 and Re=154. Simulation results of standard CFD are compared with an equivalent case with lamella stabilized, and experimental results of [58]

means the lamella does not exist in the current state of the simulation anymore and the whole algorithm 1 could be stopped in order to save-up the computational cost.

Algorithm 1: The proposed general lamella stabilization algorithm

```
for all the interface cells do
    P = current cell;
    Checking direction = Corresponding direction of max(|n_x|, |n_y|, |n_z|)_P;
    F1, F2 = neighbors of P in checking direction;
    if (φ_p > φ_F1 and φ_p > φ_F2) then
        ζ = (1.0 − φ_P);
        φ_P^new = φ_P + ζ;
    end
end
```

This algorithm is an accurate, general-purpose, case-insensitive, and computationally efficient solution to lamella stabilization problem. Figure 6 provides the quantitative comparison of the droplet radial expansion for a head-on collision of two droplets with We=269 and Re=154 (the same collision case illustrated in figure 3). The results of experimental data of Willis and Orme [58] are compared with the numerical simulations

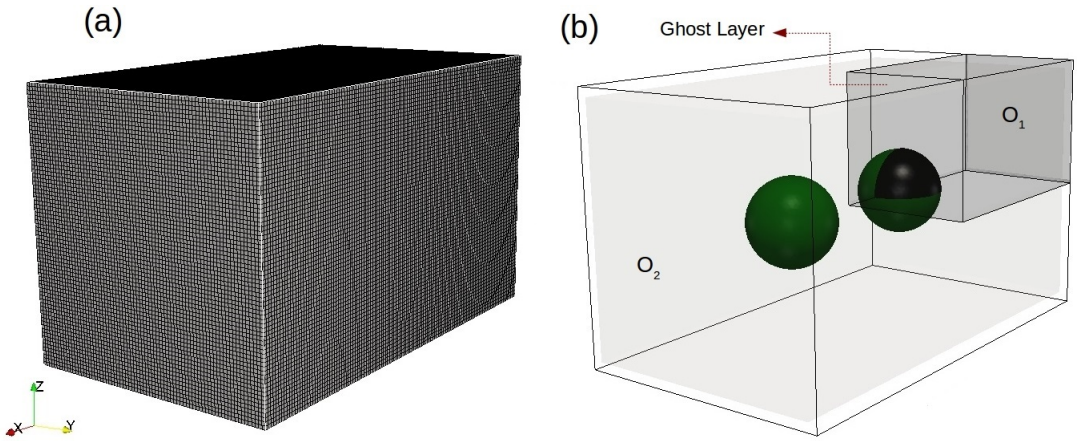

Figure 7: (a): Mesh configuration, structured cubic cells. (b): computational setup for the case that only collision of one-quarter of one droplet with ghost-nodes layer is being solved (gray domain, O_1, and black portion of the droplet) and the case that collision of two droplets is being solved (O_2).

done in this study, one with standard CFD simulation and other with proposed lamella stabilization approach in a domain with a grid size of h=D/50. It is plain to see that even for such a fine grid size, the standard CFD simulation fails in capturing the correct topology of the collision. Simulation with the proposed lamella stabilization approach, however, yields in results with good agreement compared with experimental data.

4. Results and Discussions

Two initially departed droplets in a lighter environment are being collided in a domain with length L, width W and height H in X, Y and Z directions, respectively. At the beginning of the simulation, the surrounding matrix gas is static while a uniform velocity is being imposed to the droplets giving them a relative velocity of U_{rel} in opposite directions. Characteristics of the simulations done in this study are presented in table 1. Density and viscosity ratios for all the simulations are $\rho_d/\rho_m = 666$ and $\mu_d/\mu_m = 120$, respectively. In this notation, subscript d stands for *droplet* and subscript m stands for *matrix*. These values of density and viscosity ratios are related to Tetradecane as droplet and Air as the matrix.

In this study, two different domains of O_1 and O_2 as presented in figure 7(b) are used. In the domain O_1, only one-eighth of the whole domain (O_2) is being solved. Instead of simulation of the collision of two droplets, the collision of one-fourth of only one droplet with the ghost-nodes layer, as explained in section 3.3, is being solved. Thus, ghost-nodes layer boundary condition is applied on collision plane, symmetry boundary condition is applied on the bottom and side walls (z_0 and y_0), and Neumann boundary condition is

Table 1: Characteristics of the simulations

Case	We	Re	I	$L/D_0 \times H/D_0 \times W/D_0$	$t_{rupture}/t^*$
SPC	2.3	46.83	0	2.5×1.5 × 1.5	0.7682
B	9.33	118.11	0	2.5×1.5 × 1.5	∞
HPC_1	13.63	143.6	0	2.5×1.5 × 1.5	0.8567
HPC_2	70.8	327	0.25	5.0×2.8 × 2.8	0.0
HPC_3	56.3	288.9	0.13	5.0×2.8 × 2.8	0.0
CFRS	61.4	296.5	0.06	5.0×2.8 × 2.8	0.0
$CFSS_1$	64.9	312.8	0.7	6.8×2.8 × 2.8	0.0
$CFSS_2$	48.1	270.1	0.39	5.0×2.8 × 2.8	0.0
$CFSS_3$	60.1	302.8	0.55	5.0×2.8 × 2.8	0.0
HWC	357	178	0.0	5.0×3.5 × 3.5	0.0

applied on other walls. Simulations of cases SPC, B and HPC_1, are carried out in this domain. This domain will save-up the computational costs of the simulations but could only be used for the head-on collision of equal sized droplets. In the domain O_2, the collision of two droplets is being solved. All the other cases are solved in this domain with Neumann boundary condition applied on all of its walls. Computations have been performed using a Cartesian mesh of cubic grids with the edge size of h. This mesh was generated by a constant step extrusion of the two-dimensional y-z grid along the x-axis with the step size of h. Unless otherwise is mentioned, a grid size of h=$D_0/60$ is being used to discretize the domain O_1, and a grid size of h=$D_0/35$ is being used to discretize the domain O_2.

Figure 7(a) illustrates the mesh configuration and computational setup. For all the simulations of this study, time and lengths are non-dimensionalized using $t^* = D_0/U_{rel}$ and D_0, respectively. In the next subsections, the results regarding the cases tabulated in table 1 will be presented and discussed in details. We select benchmark experimental results of Qian and Law [4] and Pan et al. [10] to validate our numerical results. These results have been used widely by the research community to validate different numerical tools. For all the cases solved in this paper, the snapshots are extracted at the same exact time as experimental figures. Besides the videos of the collision process are provided in supplementary videos. In these videos time is being non-dimensionalized using the same characteristic time of $t^* = D_0/U_{rel}$ and the color contours represent the velocity magnitude on the droplets surface[1].

4.1. Retarded permanent coalescence

Cases SPC and HPC_1 are fitting in this category, where the droplets will not coalescence immediately after their initial contact. For these cases, the rupture time of the gas film between the droplets plays a vital

[1] 0 $U_{rel}/2$

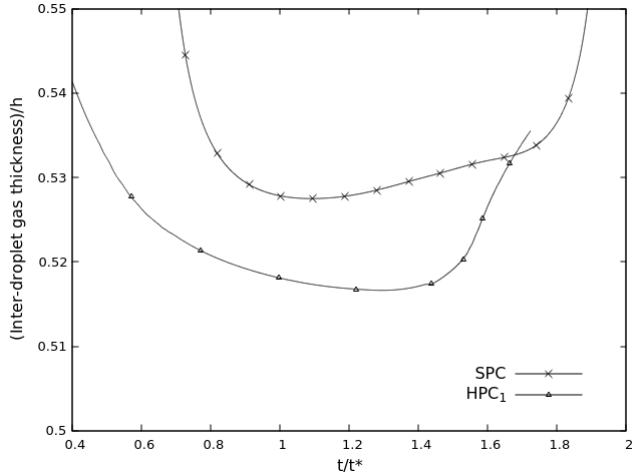

Figure 8: Non-dimensional inter-droplet gas thickness as a function of time for two bouncing cases with characteristics of cases SPC and HPC_1 of table 1

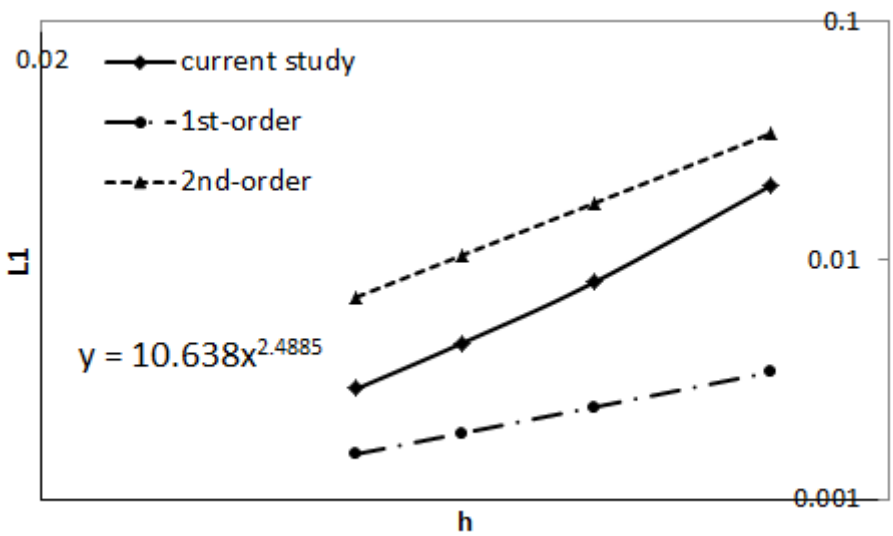

Figure 9: First norm of the error in calculation of energy budgets during the solution process of the case SPC inside of the domains with grid sizes of $h = D_0/25, D_0/35, D_0/45, D_0/55$ compared with the reference values of solution in a domain with grid size of $h = D_0/65$.

role in capturing the correct topological changes of the collision complex. This rupture time is calculated using the method explained in section 3.3. Figure 8 represents the non-dimensional inter-droplet gas film thickness as a function of time for two bouncing cases (simulations done with Dirichlet boundary condition for level-set function in the ghost-nodes layer) with characteristics as cases SPC and HPC_1. According to this figure, the bouncing simulations with characteristics of SPC and HPC_1 reach the minimum gas thickness at $t/t^* = 1.12$ and 1.25, respectively with $t/t^* = 0$ as the time when the inner-centre distance of the droplet with the ghost-nodes layer is $0.7D_0$. These values correspond to $t_{rupture}/t^* = 0.7682$ and 0.8567, respectively, with $t_{rupture}/t^* = 0$ as the time when the droplet reaches the ghost-nodes layer. With the calculated values of gas film rupture time and the method explained in section 3.3, simulations of retarded coalescence of cases SPC and HPC_1 are performed. Figures 10 and 12 illustrate the topological changes of the collision complex for these cases, extracted in the same time instances as experimental results of Pan et al. [10]. For the sake of clarity, the results extracted from domain O_1 are being reflected in X_0, Y_0 and Z_0 axes to form a whole droplet. A very good agreement is seen between the results of the current study, and the experimental results provided.

Figures 11 and 13 provide quantitative information regarding (left:) different normalized energy budgets including kinetic energy and total viscous dissipation energy inside of the droplet and matrix plus the droplet surface tension energy (hereinafter being referred as energy budget graph), (middle:) the normalized viscous dissipation rate of energy inside of the droplet and matrix (hereinafter being referred as VDR graph) and (right:) the normalized radial expansion of the droplet, Vs. non-dimensional time, for cases SPH and HPC_1, respectively. For both cases, surface tension energy is having a much higher share of the energy budget, compared with the kinetic energy of the droplet, especially for case SPH where the initial kinetic energy is almost negligible. For both cases, the surface tension energy increases as the droplet undergoes topological changes, until $t = t_{rupture}$ of the gas film, when a sudden dip in the surface tension energy is being witnessed. This sudden decrease is due to the elimination of the common surface between the droplets in the inter-droplet gas film.

Upon the coalescence of the droplets, there is a jump in viscous dissipation rate of the droplets and matrix. Since the total dissipation energy is a time-integral of the viscous dissipation rate (see equation 22), this sudden increase in it leads to a slightly delayed sudden increase in the dissipated energy for both cases. This increase compensates for the loss of surface tension energy, in the total energy of the system. Kinetic energy in the matrix for both cases is almost negligible.

A grid convergence analysis is provided on the energy budget calculations of the case SPC. Five meshes

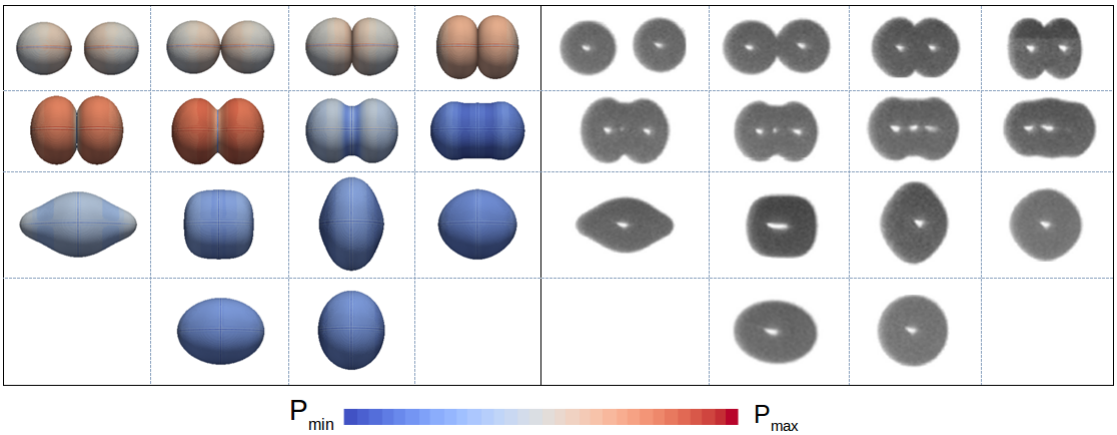

Figure 10: Topological changes of head-on binary droplets collision of case SPH in table 1. Right: experimental results of [10], Left: numerical simulation of current study with pressure contours on the droplet surface. These figures are extracted in the same time instances of experimental figures as $t/t^* = [0.0, 0.34, 0.72, 1.08, 1.12, 1.16, 1.19, 1.27, 1.60, 1.92, 2.29, 2.82, 3.44, 3.88]$ with $t/t^* = 0.0$ as the time when the droplet distance to the ghost-nodes layer is $0.7D_0$. The video of the collision process of this case is provided in supplementary material, videos SPC_a and SPC_b for side and oblique views, respectively.

with different grid sizes of $h = D_0/25, D_0/35, D_0/45, D_0/55$ and $D_0/65$ are used to solve this case. The results of the solution with the finest grid ($h = D_0/65$) are selected as the reference data and the results of other simulations are compared with them. For each case, the errors related to the different energy budgets of kinetic, surface tension and viscous dissipation at each timestep are calculated. Accumulated values of these errors are calculated as the first norm of the error using $L_1 = \sum_i |e_i|$, where e_i is the difference between energy budgets of the simulation and its corresponding value in the reference simulation at i-th iteration. Figure 9 presents the values of L_1 as a function of the grid size. As can be seen, the solution process illustrates an order of convergence of 2.48 in space. A comparison of the topological changes for solution processes done in domains with grid sizes of $h = D_0/25$ and $h = D_0/65$ are provided in supplementary figure 1.

4.2. Bouncing

Bouncing of the collided droplets corresponds to the case B of table 1. In this regime, the contact time is too short to allow the full film drainage to happens and as a result of the gas-film persistence in the inter-droplet region, the collision ends-up in bouncing. The droplet is initially placed at a distance of $0.7D_0$ with the ghost-nodes layer. The results of the simulation are illustrated in figure 14 compared with experimental

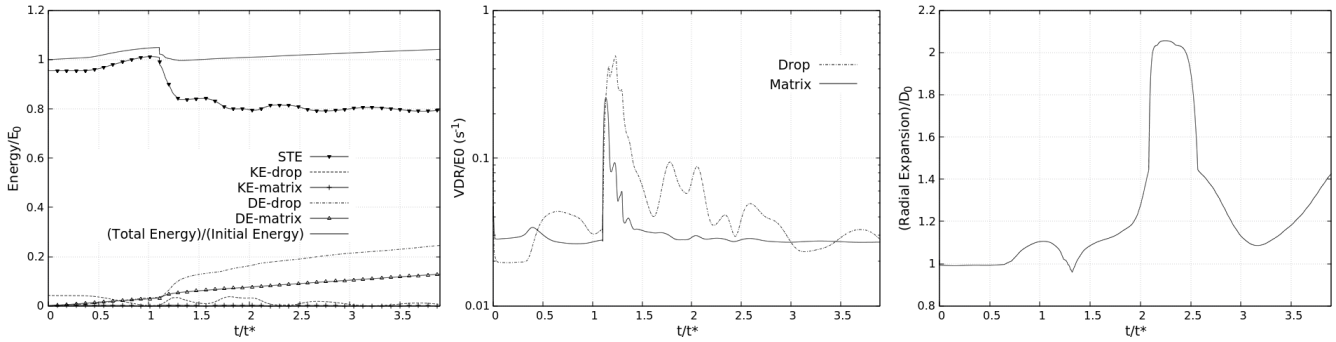

Figure 11: Left: Energy budget graph, Middle: VDR graph, Right: Normalized radial expansion of the droplet. All figure are related to case SPC of table 1 and corresponding figure of 10.

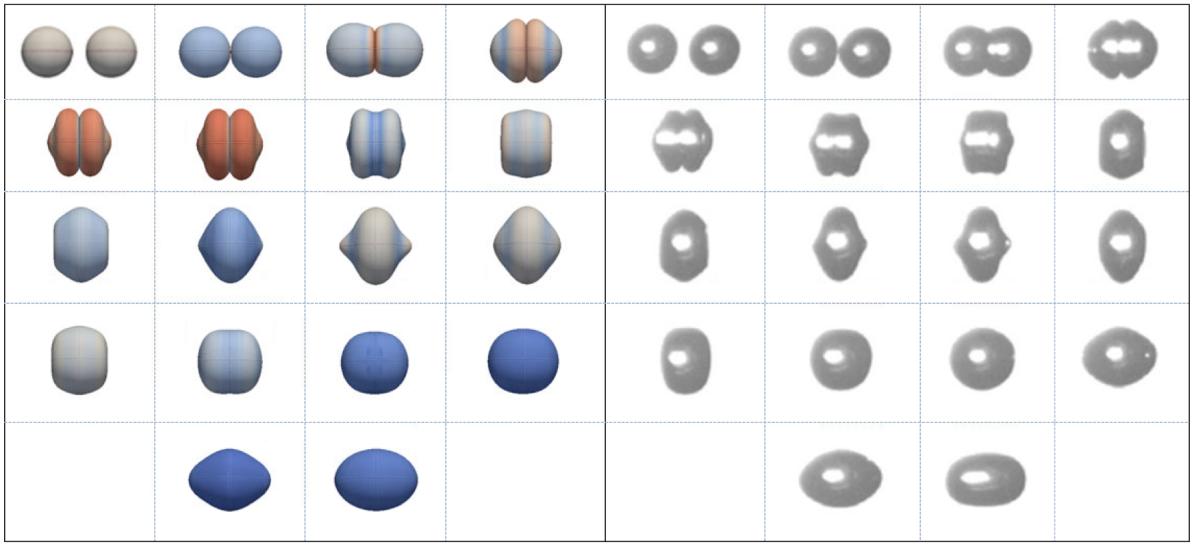

Figure 12: Topological changes of head-on binary droplet collision of case HPC_1 in table 1. Right: experimental results of [10], Left: numerical simulation of current study with pressure contours on the droplet surface. These figures are extracted in the same time instances of experimental figures as $t/t^* = [0.17, 0.38, 0.62, 1.04, 1.27, 1.28, 1.39, 1.56, 1.74, 1.91, 2.01, 2.35, 2.68, 2.99, 3.13, 3.15, 3.63, 4.0]$ with $t/t^* = 0.0$ as the time when the droplet distance to the ghost-nodes layer is $0.7D_0$. The video of the collision process of this case is provided in supplementary material, videos HPC_{1a} and HPC_{1b} for side and oblique views, respectively.

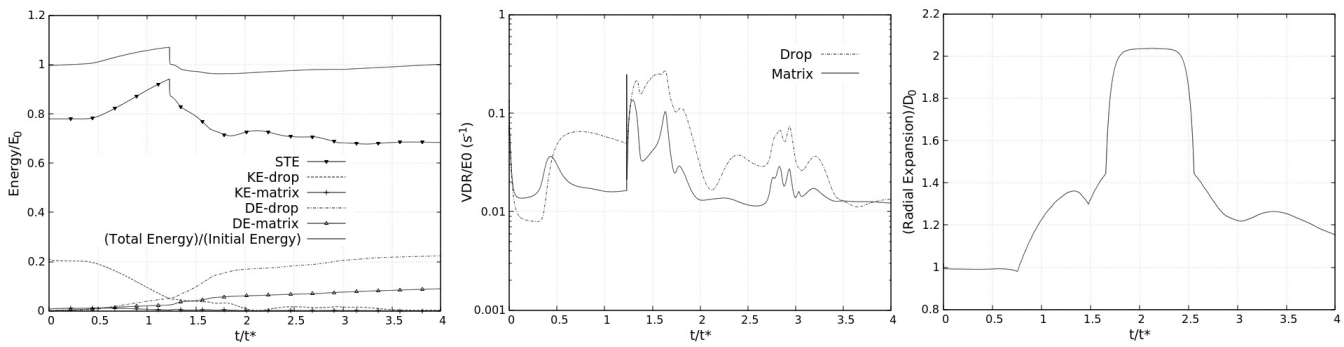

Figure 13: Left: Energy budget graph, Middle: VDR graph, Right: Normalized radial expansion of the droplet. All figure are related to case HPC_1 of table 1 and corresponding figure of 12.

results of [10] where good agreement is seen. For the sake of clarity, the results extracted from the domain O_1 are being reflected in X_0, Y_0, and Z_0 axes to form a whole droplet. Moreover, in figure 15 (left), the energy budget graph, (middle) the VDR graph and (right) normalized radial expansion of the droplet are presented. Viscous dissipation energy is almost linear with time and is more prominent in droplet compared with matrix. The kinetic energy of the matrix is almost negligible compared to other budgets of energy. Maximum viscous dissipation rate of the matrix happens around the contact time ($t/t^* \approx 0.45$) when the surface tension energy starts to increase, and kinetic energy of the droplet starts to decrease. The maximum surface tension energy, minimum kinetic energy and local minimum in viscous dissipation rate of the droplet, all happen in approximately the same time as the maximum radial expansion of the droplet. The initial budget of the kinetic energy of the droplet in bouncing regime (B), is higher than the SPH regime and is lower than the HPC_1 regime. However, the droplet kinetic energy recovery factor (KE_{final}/KE_0) for this case (regime B) is much higher than two previously studied cases (SPH and HPC_1) where the final value of kinetic energy of the droplet was almost zero. The total dissipated energy in this case is much lower than two previously studied cases of SPH and HPC_1.

4.3. Immediate permanent coalescence

Two off-center binary droplets collision cases of HPC_2 and HPC_3 of table 1 fit in the category of immediate permanent coalescence. In this regime of collision, the rupture of the gas film is very fast, resulting in immediate coalescence of the droplets. The droplets after collision retreat, and end-up in permanent coalescence. For both cases of HPC_2 and HPC_3, during the collision process, we witnessed the appearance of the lamella film. The perseverance of this film was being resolved numerically using the lamella stabilization algorithm described in section 3.4. The lamella film for cases HPC_2 and HPC_3 appears

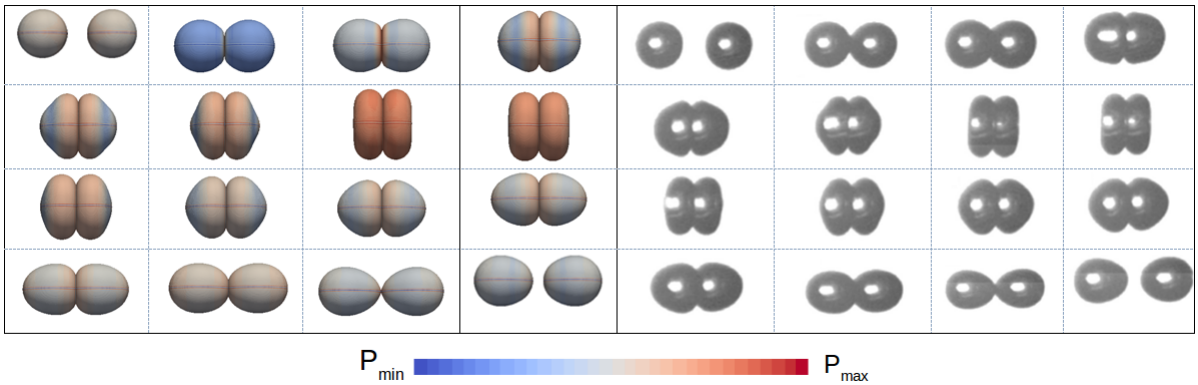

Figure 14: Topological changes of head-on binary droplet collision of case B in table 1. Right: experimental results of [10], Left: numerical simulation of current study with pressure contours on the droplet surface. These figures are extracted in the same time instances of experimental figures as $t/t^* = [0.0, 0.5, 0.58, 0.88, 1.02, 1.17, 1.43, 1.61, 1.77, 1.90, 2.05, 2.20, 2.35, 2.64, 2.89, 3.22]$ with $t/t^{=}0.0$ as the time when the droplet distance to the ghost-nodes layer is $0.7D_0$ The video of the collision process of this case is provided in supplementary material, videos B_a and B_b for side and oblique views, respectively.

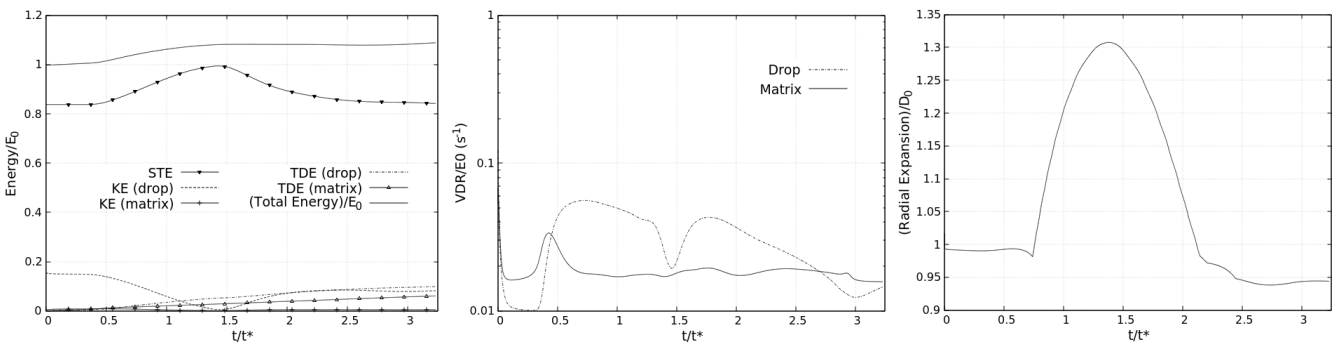

Figure 15: Left: Energy budget graph, Middle: VDR graph, Right: Normalized radial expansion of the droplet. All figure are related to case B of table 1 and corresponding figure of 14.

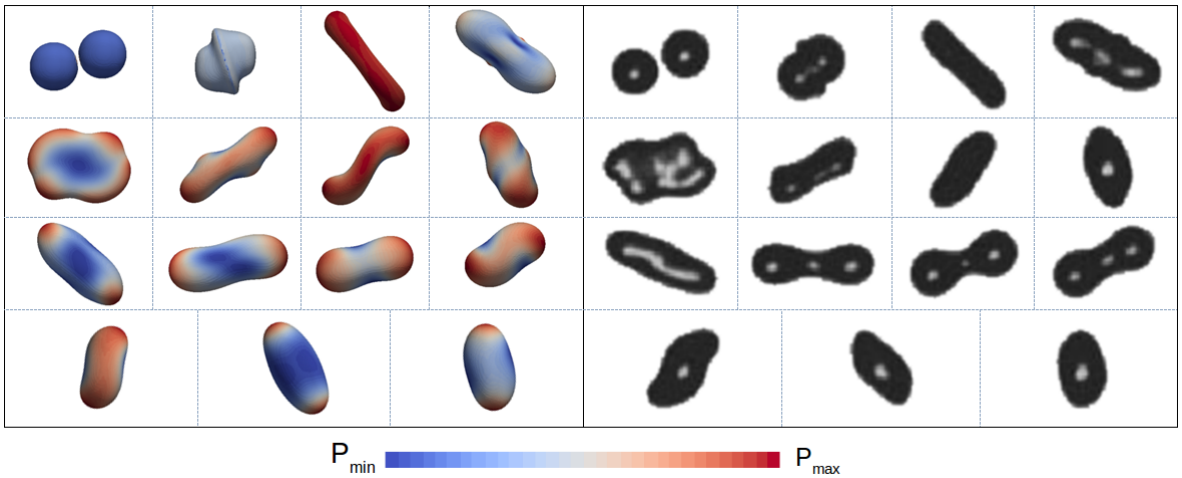

Figure 16: Topological changes of off-center binary droplets collision of case HPC_2 in table 1. Right: experimental results of [4], Left: numerical simulation of current study with pressure contours on the droplet surface. These figures are extracted in the same time instances of experimental figures as $t/t^* = [0.0, 0.32, 1.81, 2.64, 3.44, 4.35, 5.08, 5.77, 7.0, 8.78, 10.12, 10.70, 11.79, 12.92, 16.91]$ with $t/t^* = 0.0$ as the time when the droplets centerline distance in collision direction is equal to D_0. The video of the collision process of this case is provided in supplementary material, videos HPC_{2a} and HPC_{2b} for side and oblique views, respectively..

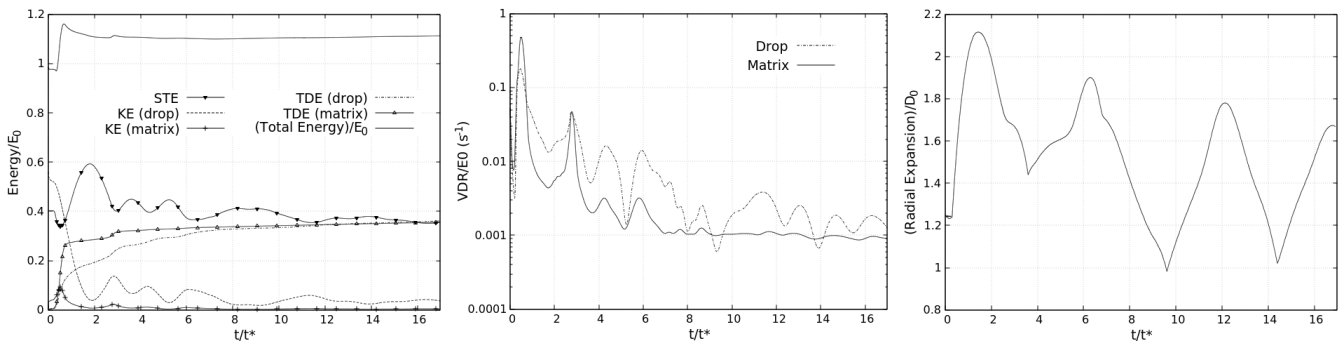

Figure 17: Left: Energy budget graph, Middle: VDR graph, Right: Normalized radial expansion of the droplet. All of these figures are related to case HPC_2 of table 1 and corresponding figure of 16.

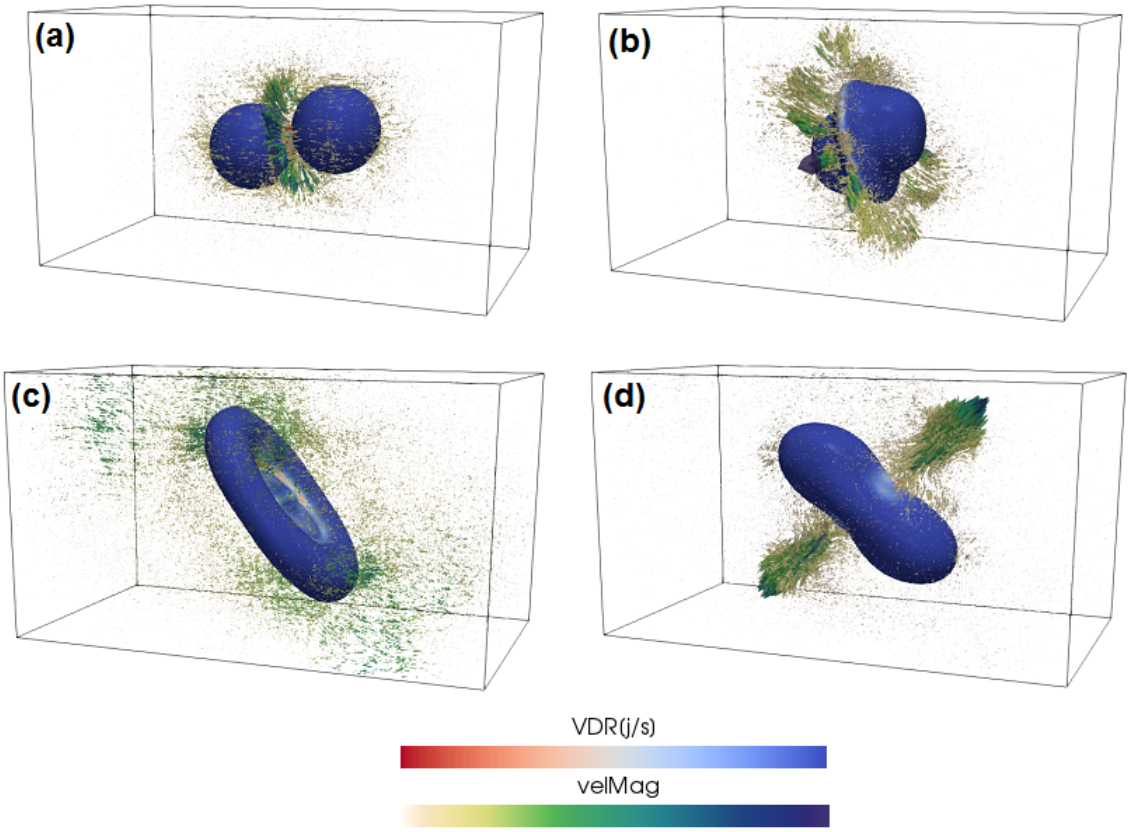

Figure 18: 3D representation of topological changes in startup collision of the case HPC_2 of table 1 and corresponding figure of 16 at times $t/t^* = [0.0, 0.32, 1.81, 2.64]$ for (a), (b), (c) and (d), respectively. The color contours on the droplet surface represent the **VDR** and the surrounding vector illustrates the velocity vectors with contours as their magnitude in the matrix.

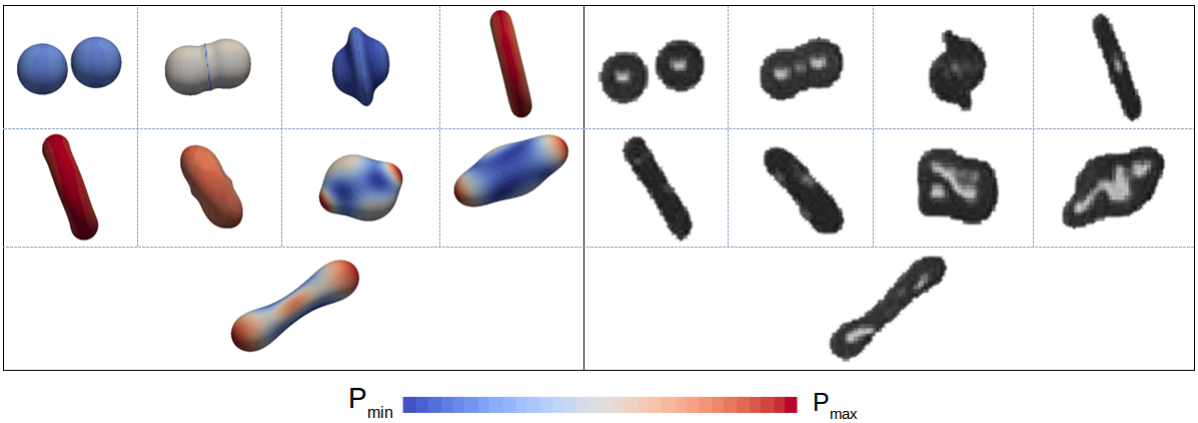

Figure 19: Topological changes of off-center binary droplet collision of case HPC_3 in table 1. Right: experimental results of [4], Left: numerical simulation of current study with pressure contours on the droplet surface. These figures are extracted in the same time instances of experimental figures as $t/t^* = [0.0, 0.16, 0.46, 1.10, 1.70, 2.31, 2.77, 3.34, 4.31]$ with $t/t^* = 0.0$ as the time when the droplets centerline distance in collision direction is equal to D_0. The video of the collision process of this case is provided in supplementary material, videos HPC_{3a} and HPC_{3b} for side and oblique views, respectively.

in time periods of $t/t^* \approx [0.32 : 2.64]$ and $t/t^* \approx [0.46 : 1.70]$, respectively. Figures 16 and 19 represents the topological changes in the collision process, compared with the experimental results of Qian and Law [4] for the same time instances where a very good agreement is seen.

Figure 17 illustrates the energy budget graph, VDR graph and normalized radial expansion of the droplets, for case HPC_2. These information for case HPC_3 are presented in supplementary figure 2.

For the case of HPC_2 represented in figure 16, since the collision is off-center with a relatively high Impact parameter of 0.25, after coalescence, the resultant droplet has bulbous which stretch in the pre-coalescence moving direction of each droplet. The kinetic energy of these bulbous is not high enough to induce breakup of the droplet. The droplet continues on stretching until the kinetic energy reaches a local minimum value at a time around $t/t^* \approx 2$. At this time, the surface tension of the resultant droplet reaches a local maximum which retreats the droplet, resulting in pulling the bulbous back in reverse direction until again the kinetic energy of the droplet reaches a local minimum. At this point, the local maximum surface tension retreats the droplet. This process continues until viscosity dissipates the energy and the resultant droplet attains a uniform spherical shape. This process induces oscillations in the deformation of the droplet and can be seen in the kinetic energy of the droplet, surface tension energy, and radial expansion of the droplet. With the lower impact parameter of the case HPC_3 (I=0.13), we will not witness the moving of

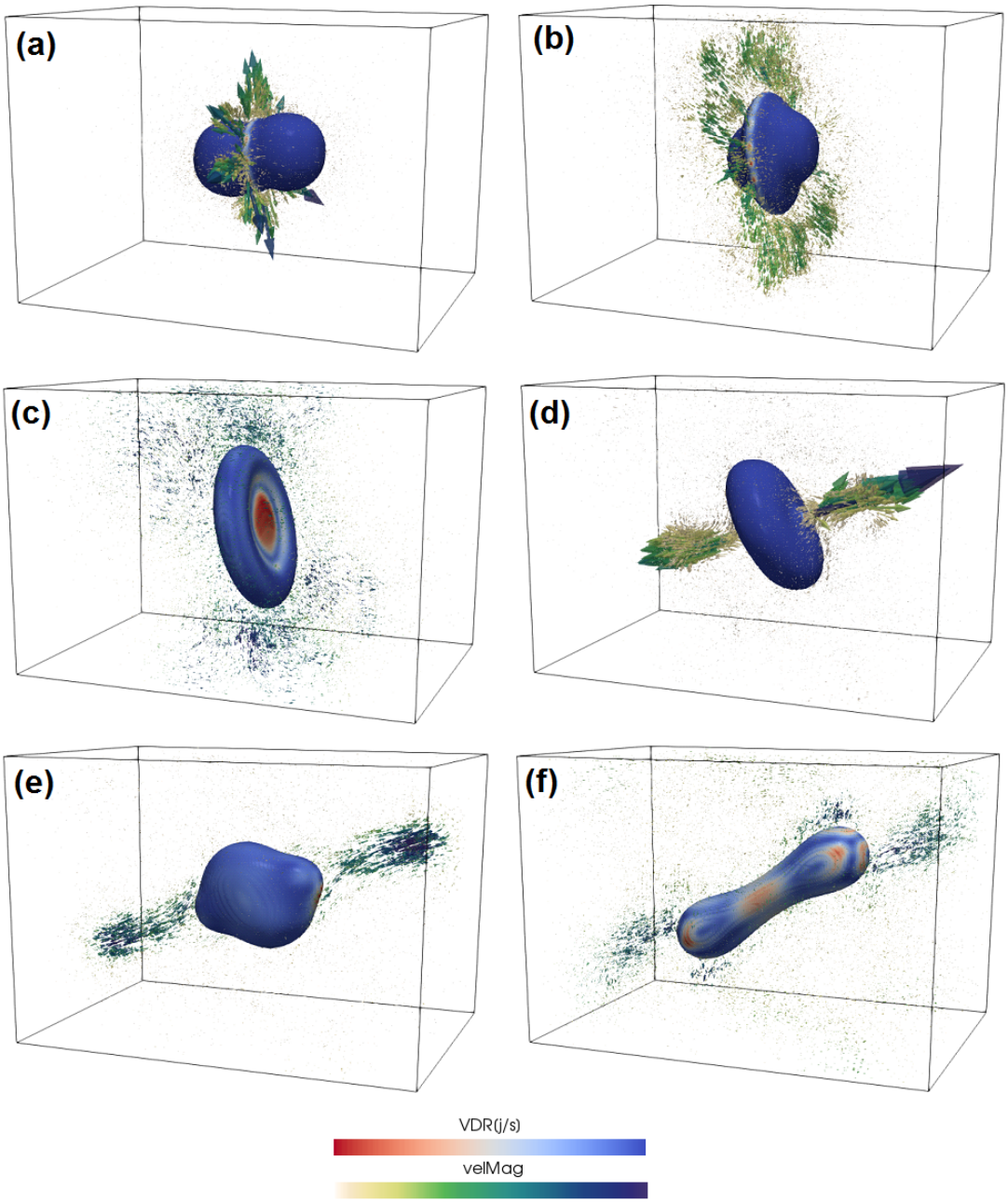

Figure 20: 3D representation of topological changes in startup collision of HPC_3 of table 1 and corresponding figure of 19 at times $t/t^* = [0.16, 0.46, 1.10, 2.31, 2.77, 4.31]$ for (a) to (f), respectively. The color contours on the droplet surface represent the **VDR** and the surrounding vector illustrates the velocity vectors with contours as their magnitude in the matrix.

the bulbous at the tips of the resultant droplet as we observed in case HPC_2. The resultant droplet does not stretch in the collision direction as much as case HPC_2, and thus the oscillations in the droplet's kinetic energy, surface tension energy, viscous dissipation rates and radial expansion of the droplet are with more prominent frequency compared with case HPC_2.

Since the type of the coalescence in these cases is immediate, the surface that is being diminished at the moment of the coalescence and as a result, the eliminated surface tension energy (the dip in the STE graph) is lower compared with the retarded coalescence cases. Around the time of the coalescence, however, there is a sudden increase in the energy dissipated in the matrix, as can be seen in figure 17 and supplementary figure 2 for cases HPC_2 and HPC_3, respectively. We believe that part of this sudden change is not physical and is a numerical artifact related to the high escape velocity of the gas in this region. Around the time of the coalescence, the gas trapped between the droplets needs to be evacuated in a short time, resulting in a very high velocity of the gas in matrix fluid. Figures 18 and 20 illustrates the topological changes in startup collision of cases HPC_2 and HPC_3, respectively. According to figure 17, there are two jumps in the viscous dissipation energy in the matrix, one for a time around the coalescence and other for $t/t^* \approx 3$. In the figure 18, we can see that for the time around coalescence (a and b), and also $t/t^* = 2.64$ the escape velocity of the gas is very high. For the case of HPC_3, the jumps in viscous dissipation energy in the matrix are in times around coalescence and $t/t^* \approx 2.5$. For this case by looking at the figure 20, we notice that the escape velocity of the gas film for times around coalescence (a and b) and also $t/t^* = 2.31$ (d) is much higher than the other times. This high sudden escape velocity of the gas introduces a very high velocity gradient in the matrix which escalates the value of the viscous dissipation energy in this zone. Accurate calculation of the velocity gradient in the matrix in this region is crucial for correct calculations of viscous dissipation energy. We believe the initial jump in the total energy of the system in these figures, is due to this problem. As could be seen in figure 17 and supplementary figure 2, there are sudden increases in the value of the viscous dissipation energy of the droplet at the same time as the matrix (around the time of coalescence) but comparably lower. We believe this jump is due to the mentioned high escape velocity of the matrix, since high escape velocity of the gas in matrix increases the velocity of nearby cells, including the droplet cells. This externally-imposed velocity gradient in the droplet results in an increase in the dissipated energy in the droplet.

This jump could be seen in the VDR graph of these cases, around the coalescence time as well. At the time of coalescence, the value of VDR for both cases in the matrix is higher than the droplet. Keeping in mind the VDF in equation 24, since the viscosity of the matrix is around 120 times lower than the

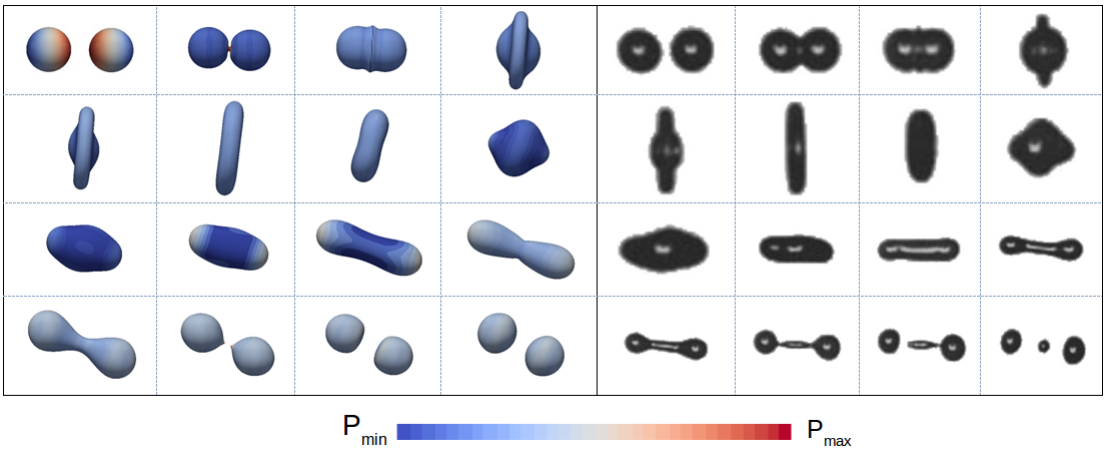

Figure 21: Topological changes of off-center binary droplet collision of case $CFRS$ in table 1. Right: experimental results of [4], Left: numerical simulation of current study with pressure contours on the droplet surface. These figures are extracted in the same time instances of experimental figures as $t/t^* = [-, 0.0, 0.29, 0.93, 1.16, 3.84, 4.54, 5.35, 7.16, 9.31, 10.47, 11.75, 12.22, 13.21, 15.95, 16.76]$ with $t/t^* = 0.0$ as the initial contact time of the droplets. The video of the collision process of this case is provided in supplementary material, video CFRS.

droplet, this higher energy dissipation rate in matrix compared to the droplet, denotes much higher velocity gradients in the matrix, compared to the droplet. These values of VDR for both matrix and droplet decrease approximately 1000 times as time passes. Another point worth mentioning is that the local minimum of viscous dissipation rate happens at the time of the local maximum of surface tension and local minimum of kinetic energies.

4.4. Coalescence followed by reflexive separation

With further increase in the Weber number, the system of droplets will experience an immediate temporary coalescence followed by a reflexive separation, as case CFRS in table 1. The separation of the droplets might be accompanied with satellite and sub-satellite droplets. Figure 21 depicts the collision outcome of the case CFRS solved in this study compared with experimental results of [4] for the same time instances. The droplets coalescence immediately after their initial contact. Thin lamella film forms for time period of $t/t^* \approx [1.16 : 4.54]$. The formation and evolution of the neck in the resultant droplet leads to the reflexive separation breakup at $t/t^* \approx 11.75$. Figure 22 represents the energy budget analysis along with the radial expansion of the collision process. Similar to the analysis of the cases in section 4.3, around the time of the coalescence, there is an immediate increase in VDR in matrix encountered by high gas escape velocity,

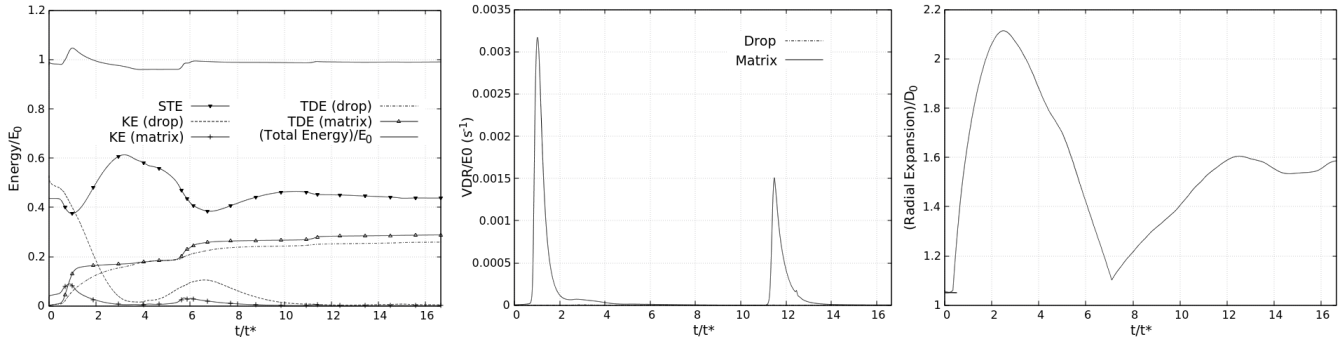

Figure 22: Left: Energy budget graph, Middle: VDR graph, Right: Normalized radial expansion of the droplet. These figures are related to the case $CFRS$ of table 1 and corresponding figure 21.

and as a result an increase in the viscous dissipation energy in the matrix. The second jump in viscous dissipation rate in matrix happens at $t/t^* \approx 6$ which is the time when the resultant droplet is being retreated, and consequently, high gas escape velocity appears in areas close to the droplet tip. These jumps in the viscous dissipation rate results in a slightly delayed jump in the dissipated energy in the matrix (figure 22 left). The value of the viscous dissipation rate in the droplet is almost negligible. These very high gas escape velocities in the matrix could be seen qualitatively in figure 23, where (a) and (b) are related to the coalescence of the droplets and (d) and (e) are related to retreatment of the resultant droplet. Upon the higher dissipated energy in the matrix, there are jumps in the kinetic energy of the matrix, one for the times around coalescence and other for the times around the retreat of the resultant droplet ($t/t^* \approx 6$). The local extrema in radial expansion of the droplet and surface tension energy happen at the same time.

4.5. Coalescence followed by stretching separation

Figures 24, 25 and 27 illustrates the collision process of binary off-center droplets in *coalescence followed by stretching separation* regime for simulations done in this paper along with the corresponding experimental results of [4] for cases $CFSS_1$, $CFSS_2$ and $CFSS_3$ of table 1. The lamella film forms in the cases of $CFSS_2$ and $CFSS_3$. According to our simulations, although in the case of $CFSS_3$, the lamella appears only for a short period during the collision process, its resolving is vital in correct capturing of the physics of the problem. High pressure in the neck right before the breakup and formation of daughter droplets are common in all the cases. Topological changes of the cases solved in this section are all in good agreement with the experimental results.

According to the experimental analysis of Qian and Law [4], which is being abstracted in figure 1, the collisions in this regime have impact parameter (I) higher than a threshold, and lower than a maximum

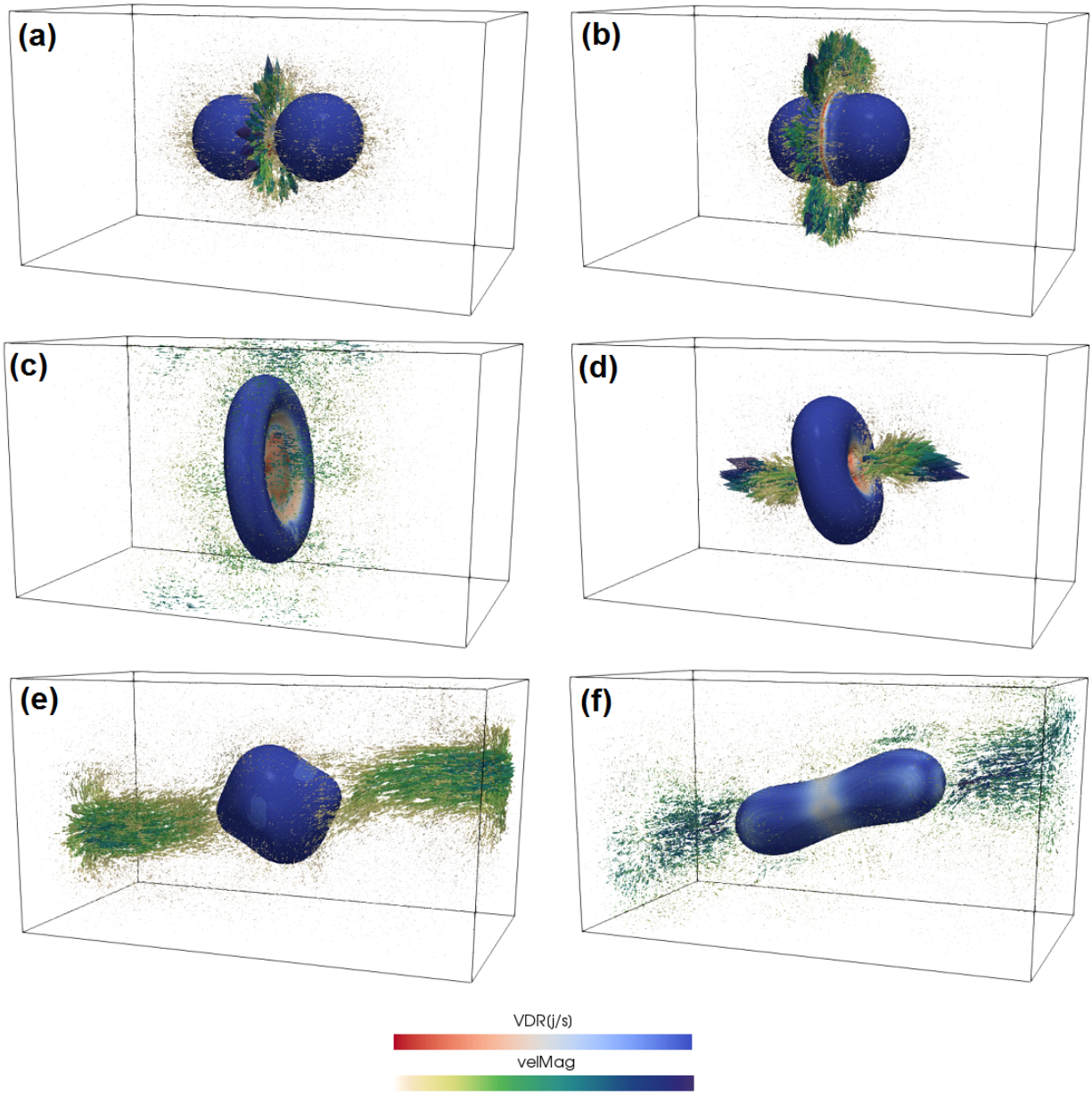

Figure 23: 3D representation of topological changes in start-up collision of case $CFRS$ of table 1 and corresponding figure of 21 at times $t/t^* = [0.0, 0.29, 3.84, 4.54, 5.35, 10.47]$ for (a) to (f), respectively. The color contours on the droplet surface represents the **VDR** and the surrounding vector illustrates the velocity vectors with contours as their magnitude in the matrix.

value. Collisions with impact parameters (I) lower than this threshold results in *hard permanent coalescence* or *coalescence followed by reflexive separation* regimes, and I values higher than the maximum, results in passing-by of the droplets with minor changes. E.g. the case $CFSS_2$ with I=0.39, is close to the regime *hard permanent coalescence* and our simulations with I value 10% smaller for this case ended-up in permanent coalescence. For this case ($CFSS_2$), the stretching of the droplet in the collision direction before breakup is smaller than the other two solved cases ($CFSS_1$ and $CFSS_3$), which is due to the smaller impact parameter of this case compared with other two cases.

Energy budgets graph along with normalized VDR and also normalized radial expansion of the droplet for case $CFSS_2$ are presented in figure 26. These information for cases $CFSS_1$ and $CFSS_3$ are provided in supplementary figures of 3 and 4. As discussed before, we observe a local maximum in the VDR graphs, around the coalescence times, resulting in a slightly delayed increase in dissipation energy both in matrix and droplet. For the case, $CFSS_1$, the kinetic energy of the droplet is not being drained totally, and it has a share of around 17% of the total energy at the end of the solution. For the case $CFSS_2$, we witness complementary oscillations in the energy budgets of surface tension energy and kinetic energy of the droplet similar to the case HPC_2 (figure 17). These oscillations happen due to the special collision characteristics. The kinetic energy stretches the resultant droplet in collision direction; thus the surplus surface tension energy retreats the resultant droplet and tries to contract it into a spherical and more stable shape which prompts overshoot in the value of the kinetic energy of the droplet. This process continues until the viscosity dissipates energy out of the system. These oscillations could be seen in the VDR of droplet and matrix as well as the radial expansion of the droplet.

4.6. High Weber collision (HWC)

In this section, the results related to the solution of a head-on binary droplet collision with a high Weber number of 357 are presented. Figure 28 illustrates the evolution of the droplets collision. Starting from the very beginning of the collision, the lamella film forms and lingers until times around $t/t^* \approx 10$. Figure 29 (right) represents the non-dimensional radial expansion of the resultant droplet, compared with the experimental data of Willis and Orme [58]. Good agreement is seen between the results of current study and the experimental data for this critical case.

Figures 29 (left) and (right) illustrates the energy budgets and VDR graphs, respectively. Contrary to the other cases presented so far, in this case, the initial share of the kinetic energy of the droplets is much higher than the initial surface tension energy. Shortly after the collision, the kinetic energy of the droplet starts to fade, and surface tension energy grows. As have been seen in previous cases, the viscous dissipation

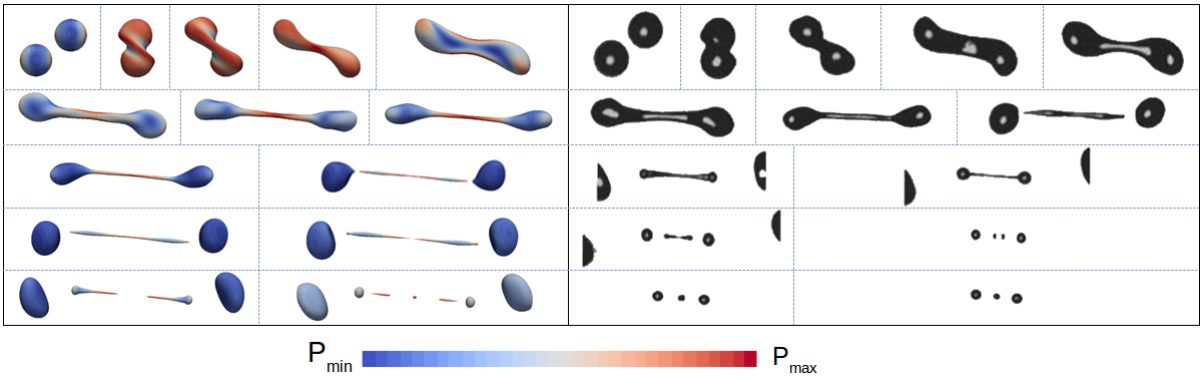

Figure 24: Topological changes of off-center binary droplets collision of the case $CFSS_1$ in table 1. Right: experimental results of [4], Left: numerical simulation of current study with pressure contours on the droplet surface. These figures are extracted in the same time instances of experimental figures as $t/t^* = [0.0, 1.05, 1.75, 2.80, 3.85, 5.25, 6.30, 7.0, 7.70, 8.75, 9.10, 9.46, 10.16, 10.86]$ with $t/t^* = 0.0$ as the time when the droplets centerline distance in collision direction is equal to D_0. The video of the collision process of this case is provided in supplementary material, videos $CFSS_{1a}$ and $CFSS_{1b}$ for side and oblique views, respectively.

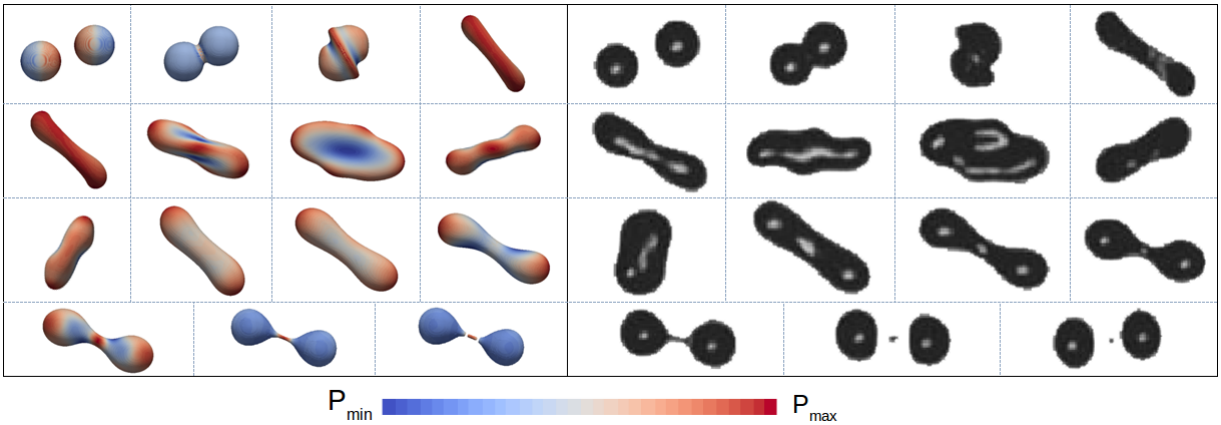

Figure 25: Topological changes of off-center binary droplet collision of case $CFSS_2$ in table 1. Right: experimental results of [4], Left: numerical simulation of current study with pressure contours on the droplet surface. These figures are extracted in the same time instances of experimental figures as $t/t^* = [0.0, 0.23, 0.53, 1.73, 2.06, 2.60, 3.17, 4.21, 4.81, 6.61, 7.20, 7.95, 8.52, 8.91, 9.54]$ with $t/t^* = 0.0$ as the time when the droplets centerline distance in collision direction is equal to $1.32D_0$. The video of the collision process of this case is provided in supplementary material, videos $CFSS_{2a}$ and $CFSS_{2b}$ for side and oblique views, respectively.

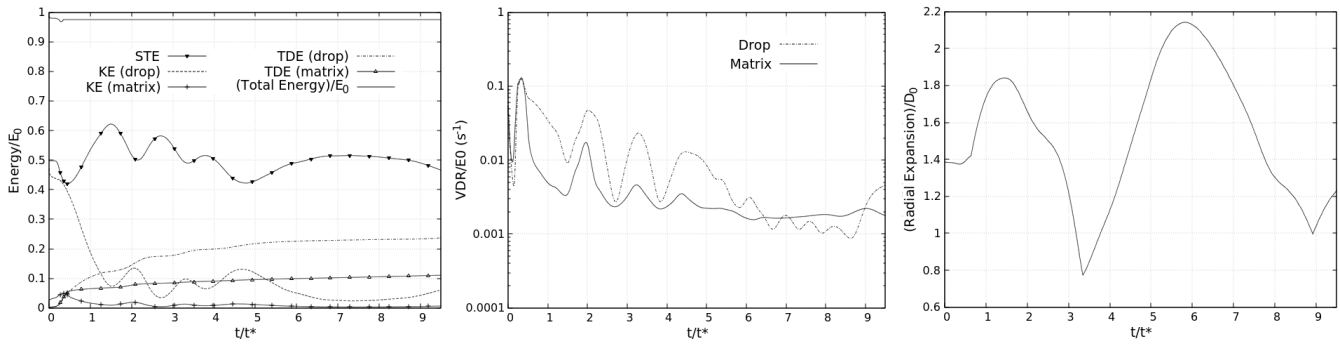

Figure 26: Left: Energy budget graph, Middle: VDR graph, Right: Normalized radial expansion of the droplet. These figures are related to the case $CFSS_2$ of table 1 and corresponding figure 25.

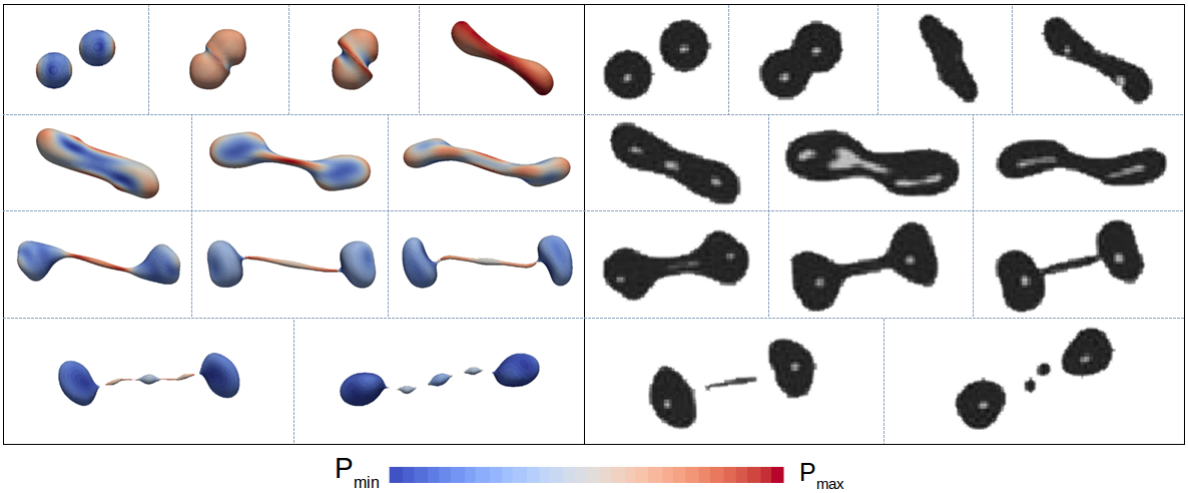

Figure 27: Topological changes of off-center binary droplet collision of case $CFSS_3$ in table 1. Right: experimental results of [4], Left: numerical simulation of current study with pressure contours on the droplet surface. These figures are extracted in the same time instances of experimental figures as $t/t^* = [0.0, 0.29, 0.43, 1.65, 2.05, 2.85, 3.21, 4.34, 4.77, 5.14, 5.63, 6.36, 8.12]$ with $t/t^* = 0.0$ as the time when the droplets centerline distance in collision direction is equal to D_0. The video of the collision process of this case is provided in supplementary material, videos $CFSS_{3a}$ and $CFSS_{3b}$ for side and oblique views, respectively.

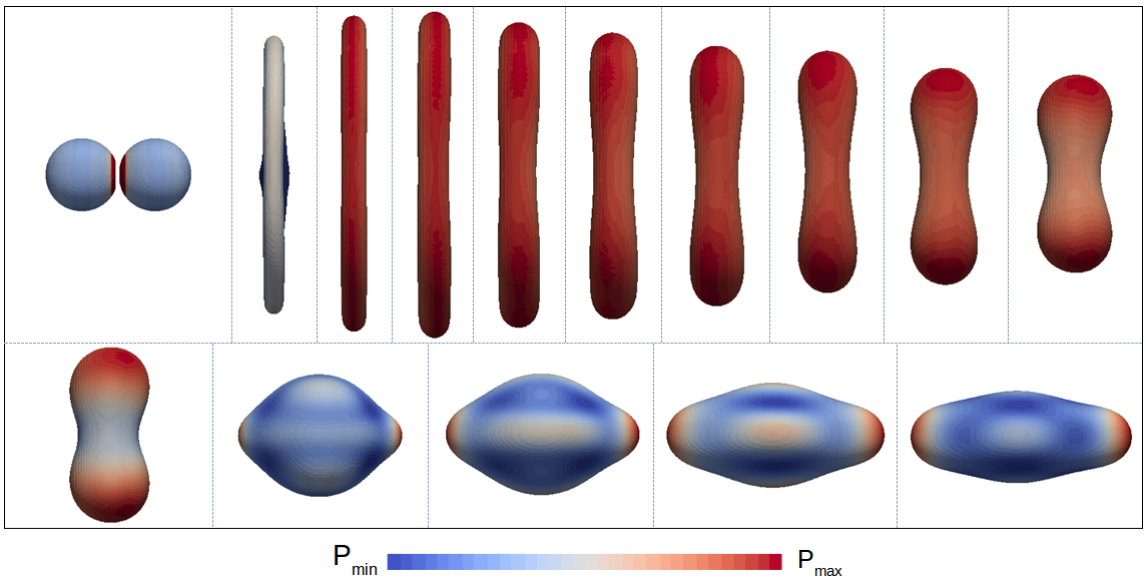

Figure 28: Snapshots of topological changes of numerical simulation of current study with pressure contours on the droplet surface for head-on binary droplet collision of case HWC in table 1. These figures are extracted in times of $t/t^* = [0.0, 2.83, 4.25, 6.02, 7.80, 8.85, 9.92, 10.63, 11.70, 12.62, 13.55, 16.52, 17.6, 18.53, 20.0]$ with $t/t^* = 0.0$ as the time when the droplets initial contact happens. The video of the collision process of this case is provided in supplementary material, videos HWC_a and WHC_b for side and oblique views, respectively..

rate is maximum around the coalescence time. The jump in the viscous dissipation energy in the matrix and droplet happens around the coalescence time as well. According to the conclusion that we made earlier, this is due to the high escape gas velocity in the matrix around the coalescence time. Supplementary figure 5 illustrates a three-dimensional representation of the topological changes in startup behavior of the collision complex of this case with color contours on the droplet surface as a representation of the **VDR** and the surrounding vector as the velocity vectors in the matrix.

5. Conclusion

Direct numerical simulation of head-on and off-center binary droplets collision in all the regimes as initially introduced by Qian and Law [4] is performed using a conservative level-set method. The snapshots of evolution of the collision process are extracted and compared with available experimental data in the literature. Very good agreement is seen between the results of current study, and available experimental data. A novel lamella stabilization approach has been introduced which numerically resolves the lamella

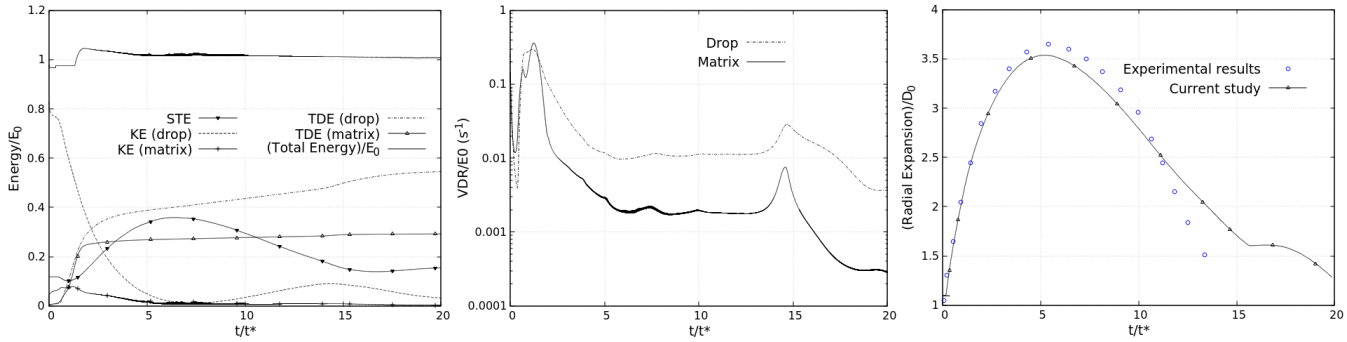

Figure 29: Left: Energy budget graph, Middle: VDR graph, Right: Normalized radial expansion of the resultant droplet compared with the experimental results of [58]. These figures are related to case HWC of table 1 and corresponding figure 28.

film, independent of its formation direction. A new ghost-nodes layer approach is proposed to prevent adding mass into the droplet. This ghost-nodes layer was used to extract the gas-film rupture time for the cases of retarded coalescence. A very profound energy analysis is provided for each case covering the a wide range of collision regimes which provides more insight into the collision process. According to the extracted results, the time and number of peaks and fluctuations of the surface tension energy are in qualitative agreement with the radial expansion of the droplets. The budget of matrix kinetic energy in all the cases is very small compared to kinetic energy of droplet, surface tension energy and viscous dissipation energy. The main gain in the kinetic energy of the matrix comes from the escape of the gas film in the matrix when the droplets approach each other around the time of the coalescence and also when the resultant droplet expands after a major retreatment. The share of viscous dissipation energy of the matrix in the cases of coalescence followed by stretching separation is lower than the viscous dissipation energy of the droplet. This norm is reverse for all the other cases. Retreat in the collision process happens when the resultant droplet reaches the local minimum kinetic energy and surface tension reaches a local maximum value. At this time, the surplus surface tension energy mobilizes the resultant droplet causing an increase in the kinetic energy. Droplet kinetic energy recovery factor (KE_{final}/KE_0) is maximum for the bouncing regime (B). The total dissipated energy in this case is also minimum among all other regimes.

Appendix A. Conservation of total energy and the role of flux-limiters

Finite volume flux-limiters schemes as introduced in Balcázar et al. [40, 61] are used for the discretization of convective terms, in order to avoid the spurious oscillations that would otherwise occur with high order

spatial discretization schemes due to discontinuities imposed by level-set function across the interface. The formulations used in this research are the so-called Minmod, Sweby, Smart, Superbee, and Van-Leer limiters [62, 63]. In this formulation, the value of variable Ψ at the cell face (Ψ_f) is written as the sum of a diffusive first-order upwind part and an anti-diffusive term as [40, 61]:

$$\Psi_f = \Psi_C + \frac{1}{2} L(\theta_f) \left(\Psi_D - \Psi_C\right) \tag{A.1}$$

The anti-diffusive part is multiplied by the flux limiter $L(\theta_f)$ with θ_f defined as the upwind ratio of the consecutive gradients of Ψ.

$$L(\theta) = \begin{cases} max\left[0, min\left(1, \theta\right)\right], & Minmod \\ max\left[0, min\left(\beta\theta, 1\right), min\left(\theta, \beta\right)\right], & Sweby \\ max\left[0, min\left(2\theta, \left(0.25 + 0.75\theta\right), 4\right)\right], & Smart \\ max\left[0, min\left(2\theta, 1\right), min\left(2, \theta\right)\right], & Superbee \\ \left(\theta + |\theta|\right) / \left(1 + |\theta|\right), & Van - Leer \\ 0.0, & Upwind \end{cases} \tag{A.2}$$

where parameter β in Sweby flux-limiter is equal to 1. In order to study the effect of different flux-limiters on conservation of total energy in the system, and choose the most consistent one, we perform numerical simulation of a droplet oscillation test case as initially solved by Mashayek and Ashgriz [64]. The test case includes the damping oscillation of a droplet released from its static condition at third mode, meaning the surface of the drop is initially perturbed from its spherical shape according to following spherical harmonics in the (r-z) coordinate system as:

$$h_{t=0}(\theta) = R_3 \left(1 + 0.25 \left(5cos^3\theta - 3cos\theta\right)\right) \tag{A.3}$$

in this formulation, the amplitude of the initial perturbation is equal to 0.5, R_3 is used to maintain the volume of the droplet constant during the initial perturbation and is equal to 0.966. Simulations are done in Reynolds number of 100, with $Re = \sqrt{\sigma r_0 \rho_l}/\mu_l$. Figure A.30 illustrates the coordinate system along with the initial shape of the perturbed droplet. Two-dimensional simulation domain has length and height of $6r_0$, with r_0 as the initial radius of the droplet. A density ratio and of $\rho_d/\rho_m = 1000$ and viscosity ratio of $\mu_d/\mu_m = 400$ are applied. Time is being non-dimensionalized using $t^* = \sqrt{\rho_d r_0^3/\sigma}$. Simulations

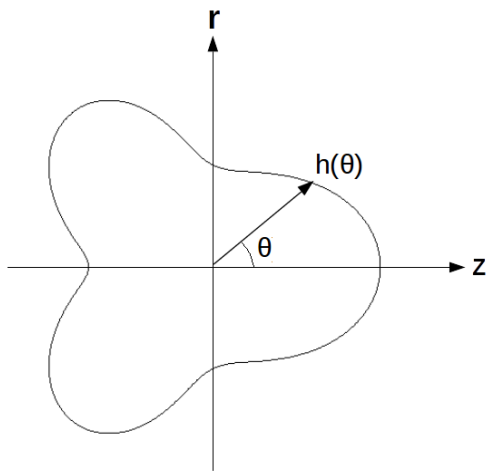

Figure A.30: Schematic of the 2D droplet oscillation problem.

Table A.2: Total energy conservation error of the droplet oscillation case of Appendix A for solutions with different flux-limiters.

Flux-limiter	Minmod	Sweby	Smart	Superbee	Van Leer
ΔE	0.0612	0.0202	-0.0310	0.0153	0.0376

are done until $t/t^* = 13.7$ with a constant timestep of $dt/t^* = 3.87 \times 10^{-4}$ for all the cases. A grid size of $h = 2r_0/35$ is used for all the cases unless otherwise is mentioned. Simulations are done with different flux-limiters. For each case, the error in total energy conservation at the end of the simulation is calculated as $\Delta E = |E_{final} - E_{init}|/E_{init}$ where E_{final} and E_{init} are final and initial values of total energy of the system. Table A.2 represent this criteria for different flux-limiters tested in this section. According to this table, it is plain to see that the Superbee flux-limiter has lower error in conservation of the energy of the system and thus is more suitable in energy analysis study of this paper. For the case where Upwind scheme is being applied on convective terms in the whole domain, the value of ΔE is 0.17 which is comparably higher than equivalent value of any other flux-limiter.

Figure A.31 represents the results extracted in this study solved with Superbee flux limiter, compared with the reference data extracted in the same time instances. A.32 illustrates the normalized energy budget of STE, KE, and TDE for droplet and matrix for the solution with Superbee flux-limiter. In this figure, the oscillations in kinetic energy of droplet, surface tension energy, and DE in matrix could be seen. Good conservation of total energy of the system is seen in this figure as well.

In order to analyze the spacial accuracy convergence of the total energy conservation, simulations of this

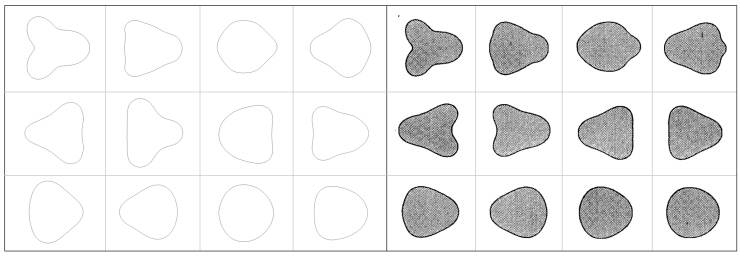

Figure A.31: Time evolution of the oscillations in droplet deformation for droplet with initial perturbation as described in Appendix A. Left: result extracted in current study with Superbee flux limiter. Right: reference data of [64]. The snapshots are extracted in the same time instant as $t/t^* = [0.0, 0.2, 0.35, 0.48, 0.63, 1.42, 1.94, 2.74, 4.10, 5.90, 8.90, 10.10]$.

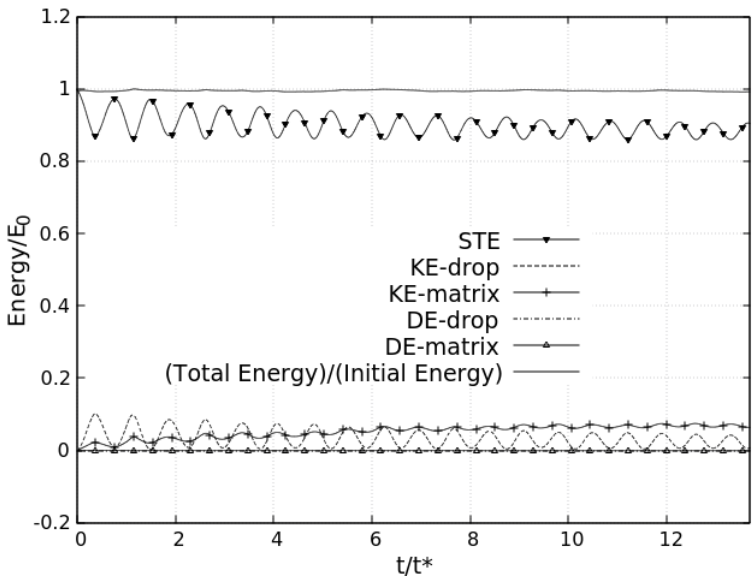

Figure A.32: Normalized energy budget of STE, KE, and TDE for droplet and matrix fluids.

case with Superbee flux-limiter with different grid sizes of $h = 2r_0/25, 2r_0/35$ and $2r_0/45$ are performed. A constant timestep is used for all the simulations. In each case, the ΔE error as mentioned earlier is calculated. In the imaginary perfect solution, the value of ΔE must be equal to zero. According to the results extracted, for the performed droplet oscillation case of this section, the error in total energy conservation of the system has a convergence rate of 1.74 in space.

Acknowledgments

This work has been financially supported by the *Ministerio de Economía y Competitividad, Secretaría de Estado de Investigación, Desarrollo e Innovación*, Spain (ENE2015-70672-P). A. Amani acknowledges the financial support of an FI research scholarship by the *Agència de Gestió d'Ajuts Universitaris i de Recerca (AGAUR) of Generalitat de Catalunya* (2016 FI_B 01059). N. Balcázar acknowledges the financial support of the Programa Torres Quevedo (PTQ-14-07186). The authors thankfully acknowledge the computer resources at Altamira and the technical support provided by Instituto de Física de Cantabria - Universidad de Cantabria (RES-FI-2018-3-0045).

References

1. Dudukovic MP, Larachi F, Mills PL. Multiphase reactors - revisited. *Chemical Engineering Science* 1999;54(13-14):1975–95. doi:10.1016/S0009-2509(98)00367-4.
2. Hu Z, Srivastava RC. Evolution of Raindrop Size Distribution by Coalescence, Breakup, and Evaporation: Theory and Observations. *Journal of the Atmospheric Sciences* 1995;52(10):1761–83. URL: https://doi.org/10.1175/1520-0469(1995)052%3C1761:EORSDB%3E2.0.CO;2. doi:10.1175/1520-0469(1995)052<1761:EORSDB>2.0.CO;2.
3. Ashgriz N, Poo JY. Coalescence and separation in binary collisions of liquid drops. *Journal of Fluid Mechanics* 1990;221:183–204. doi:10.1017/S0022112090003536.
4. Qian J, Law CK. Regimes of coalescence and separation in droplet collision. *Journal of Fluid Mechanics* 1997;331:59–80. doi:10.1017/S0022112096003722.
5. Planchette C, Lorenceau E, Brenn G. Binary collisions of immiscible liquid drops for liquid encapsulation. *Fluid Dynamics and Materials Processing* 2011;7(3):279–302. doi:10.3970/fdmp.2011.007.279.
6. Brazier-Smith PR, Jennings SG, Latham J. The Interaction of Falling Water Drops: Coalescence. *Proceedings of the Royal Society A: Mathematical, Physical and Engineering Sciences* 1972;326(1566):393–408. URL: http://rspa.royalsocietypublishing.org/cgi/doi/10.1098/rspa.1972.0016. doi:10.1098/rspa.1972.0016.
7. Brenn G, Frohn A. Collision and coalescence of droplets of various liquids. *Journal of Aerosol Science* 1989;20(8):1027–30. URL: http://www.sciencedirect.com/science/article/pii/0021850289907532. doi:https://doi.org/10.1016/0021-8502(89)90753-2.
8. Jiang YJ, Umemura A, Law CK. An experimental investigation on the collision behaviour of hydrocarbon droplets. *Journal of Fluid Mechanics* 1992;234:171–90. doi:10.1017/S0022112092000740.

9. Willis KD, Orme ME. Experiments on the dynamics of droplet collisions in a vacuum. *Experiments in Fluids* 2000;29(4):347–58. URL: https://doi.org/10.1007/s003489900092. doi:10.1007/s003489900092.
10. Pan KL, Law CK, Zhou B. Experimental and mechanistic description of merging and bouncing in head-on binary droplet collision. *Journal of Applied Physics* 2008;103(6). doi:10.1063/1.2841055.
11. Tang C, Zhang P, Law CK. Bouncing, coalescence, and separation in head-on collision of unequal-size droplets. *Physics of Fluids* 2012;24(2). doi:10.1063/1.3679165.
12. Pan KL, Chou PC, Tseng YJ. Binary droplet collision at high Weber number. *Physical Review E - Statistical, Nonlinear, and Soft Matter Physics* 2009;80(3):1–8. doi:10.1103/PhysRevE.80.036301.
13. Planchette C, Hinterbichler H, Liu M, Bothe D, Brenn G. Colliding drops as coalescing and fragmenting liquid springs. *Journal of Fluid Mechanics* 2017;814:277–300. doi:10.1017/jfm.2016.852.
14. Pan KL, Tseng YH, Chen JC, Huang KL, Wang CH, Lai MC. Controlling droplet bouncing and coalescence with surfactant. *Journal of Fluid Mechanics* 2016;799:603–36. doi:10.1017/jfm.2016.381.
15. Estrade JP, Carentz H, Lavergne G, Biscos Y. Experimental investigation of dynamic binary collision of ethanol droplets - a model for droplet coalescence and bouncing. *International Journal of Heat and Fluid Flow* 1999;20(5):486–91. doi:10.1016/S0142-727X(99)00036-3.
16. Reitz TLG, D. R. A DROP-SHATTERING COLLISION MODEL FOR MULTIDIMENSIONAL SPRAY COMPUTATIONS. *Atomization and Sprays* 1999;9(1044-5110):231–54.
17. Gopinath Arvind Koch DL. Collision and rebound of small droplets in an incompressible continuum gas. *Journal of Fluid Mechanics* 2002;454:145âĂŞ201. doi:10.1017/S0022112001006966.
18. Bach GA, Koch DL, Gopinath A. Coalescence and bouncing of small aerosol droplets. *Journal of Fluid Mechanics* 2004;518:157âĂŞ185. doi:10.1017/S0022112004000928.
19. Zhang P, Law CK. An analysis of head-on droplet collision with large deformation in gaseous medium. *Physics of Fluids* 2011;23(4). doi:10.1063/1.3580754.
20. Li J. Macroscopic model for head-on binary droplet collisions in a gaseous medium. *Physical Review Letters* 2016;117(21):1–5. doi:10.1103/PhysRevLett.117.214502.
21. Nikolopoulos N, Bergeles G. The effect of gas and liquid properties and droplet size ratio on the central collision between two unequal-size droplets in the reflexive regime. *International Journal of Heat and Mass Transfer* 2011;54(1-3):678–91. URL: http://dx.doi.org/10.1016/j.ijheatmasstransfer.2010.09.002. doi:10.1016/j.ijheatmasstransfer.2010.09.002.
22. Nikolopoulos N, Theodorakakos A, Bergeles G. Off-centre binary collision of droplets: A numerical investigation. *International Journal of Heat and Mass Transfer* 2009;52(19-20):4160–74. doi:10.1016/j.ijheatmasstransfer.2009.04.011.
23. Chen X, Ma D, Khare P, Yang V. Energy and Mass Transfer during Binary Droplet Collision. In: *49th AIAA Aerospace Sciences Meeting including the New Horizons Forum and Aerospace Exposition*. Aerospace Sciences Meetings; American Institute of Aeronautics and Astronautics; 2011:URL: https://doi.org/10.2514/6.2011-771. doi:doi:10.2514/6.2011-771.
24. Pan Y, Suga K. Numerical simulation of binary liquid droplet collision. *Physics of Fluids* 2005;17(8):1–14. doi:10.1063/1.2009527.
25. Tanguy S, Berlemont A. Application of a level set method for simulation of droplet collisions. *International Journal of Multiphase Flow* 2005;31:1015–35. URL: http://linkinghub.elsevier.com/retrieve/pii/S0301932205000832. doi:10.1016/j.ijmultiphaseflow.2005.05.010.
26. Kwakkel M, Breugem WP, Boersma BJ. Extension of a CLSVOF method for droplet-laden flows with a coales-

cence/breakup model. *Journal of Computational Physics* 2013;253:166–88. doi:10.1016/j.jcp.2013.07.005.

27. Balcázar N, Lehmkuhl O, Rigola J, Oliva A. A multiple marker level-set method for simulation of deformable fluid particles. *International Journal of Multiphase Flow* 2015;74:125–42. doi:10.1016/j.ijmultiphaseflow.2015.04.009.
28. Nobari MR, Jan YJ, Tryggvason G. Head-on Collisions of Drops - A Numerical Investigation. *Physics of Fluids* 1996;8(1):29–42.
29. Zhang Z, Zhanga P. Kinetic energy recovery and interface hysteresis of bouncing droplets after inelastic head-on collision. *Physics of Fluids* 2017;29(10). doi:10.1063/1.5000547.
30. Lycett-Brown D, Luo KH, Liu R, Lv P. Binary droplet collision simulations by a multiphase cascaded lattice Boltzmann method. *Physics of Fluids* 2014;26(2). doi:10.1063/1.4866146.
31. Moqaddam AM, Chikatamarla SS, Karlin IV. Simulation of binary droplet collisions with the entropic lattice Boltzmann method. *Physics of Fluids* 2016;28(2). URL: http://dx.doi.org/10.1063/1.4942017. doi:10.1063/1.4942017.
32. Premnath KN, Abraham J. Simulations of binary drop collisions with a multiple-relaxation-time lattice-Boltzmann model. *Physics of Fluids* 2005;17(12):1–21. doi:10.1063/1.2148987.
33. Dupuy PM, Lin Y, Fernandino M, Jakobsen HA, Svendsen HF. Modelling of high pressure binary droplet collisions. *Computers and Mathematics with Applications* 2011;61(12):3564–76. doi:10.1016/j.camwa.2010.05.044.
34. Baroudi L, Kawaji M, Lee T. Effects of initial conditions on the simulation of inertial coalescence of two drops. *Computers and Mathematics with Applications* 2014;67(2):282–9. doi:10.1016/j.camwa.2013.05.002.
35. Sun K, Jia M, Wang T. Numerical investigation on the head-on collision between unequal-sized droplets with multiple-relaxation-time lattice Boltzmann model. *International Journal of Heat and Mass Transfer* 2014;70:629–40. URL: http://dx.doi.org/10.1016/j.ijheatmasstransfer.2013.11.055. doi:10.1016/j.ijheatmasstransfer.2013.11.055.
36. Mazloomi AM, Chikatamarla SS, Karlin IV. Entropic Lattice Boltzmann Method for Multiphase Flows. *Physical Review Letters* 2015;114(17):174502. doi:10.1103/PhysRevLett.114.174502.
37. Lycett-Brown D, Luo KH. Cascaded lattice Boltzmann method with improved forcing scheme for large-density-ratio multiphase flow at high Reynolds and Weber numbers. *Physical Review E* 2016;94(5):1–20. doi:10.1103/PhysRevE.94.053313.
38. Monaco E, Brenner G, Luo KH. Numerical simulation of the collision of two microdroplets with a pseudopotential multiple-relaxation-time lattice Boltzmann model. *Microfluidics and Nanofluidics* 2014;16(1-2):329–46. doi:10.1007/s10404-013-1202-0.
39. Zhang YR, Jiang XZ, Luo KH. Bounce regime of droplet collisions: A molecular dynamics study. *Journal of Computational Science* 2016;17:457–62. URL: http://dx.doi.org/10.1016/j.jocs.2016.03.011. doi:10.1016/j.jocs.2016.03.011.
40. Balcazar N, Jofre L, Lehmkuhl O, Castro J, Rigola J. A finite-volume/level-set method for simulating two-phase flows on unstructured grids. *International Journal of Multiphase Flow* 2014;64:55–72. doi:10.1016/j.ijmultiphaseflow.2014.04.008.
41. Balcázar N, Lehmkuhl O, Jofre L, Rigola J, Oliva A. A coupled volume-of-fluid/level-set method for simulation of two-phase flows on unstructured meshes. *Computers & Fluids* 2016;124:12–29. URL: http://www.sciencedirect.com/science/article/pii/S0045793015003394. doi:10.1016/j.compfluid.2015.10.005.
42. Balcázar N, Castro J, Rigola J, Oliva A. DNS of the wall effect on the motion of bubble swarms. In: *Procedia Computer Science*; vol. 108. 2017:2008–17. doi:10.1016/j.procs.2017.05.076.
43. Olsson E, Kreiss G. A conservative level set method for two phase flow. *Journal of Computational Physics* 2005;210(1):225–

46. URL: http://www.sciencedirect.com/science/article/pii/S0021999105002184. doi:http://dx.doi.org/10.1016/j.jcp.2005.04.007.

44. Brackbill JU, Kothe DB, Zemach C. A continuum method for modeling surface tension. *Journal of Computational Physics* 1992;100(2):335–54. URL: http://www.sciencedirect.com/science/article/pii/002199919290240Y. doi:http://dx.doi.org/10.1016/0021-9991(92)90240-Y.

45. Chorin AJ. Numerical solution of the Navier-Stokes equations. *Mathematics of Computation* 1968;22(104):745–. URL: http://www.ams.org/jourcgi/jour-getitem?pii=S0025-5718-1968-0242392-2. doi:10.1090/S0025-5718-1968-0242392-2.

46. Gottlieb S, Shu CW. Total variation diminishing Runge-Kutta schemes. *Mathematics of computation of the American Mathematical Society* 1998;67(221):73–85.

47. Rhie CM, Chow WL. Numerical study of the turbulent flow past an airfoil with trailing edge separation. *AIAA journal* 1983;21(11):1525–32.

48. Balcázar N, Rigola J, Castro J, Oliva A. A level-set model for thermocapillary motion of deformable fluid particles. *International Journal of Heat and Fluid Flow* 2016;62(Part B):324–43. URL: http://www.sciencedirect.com/science/article/pii/S0142727X16301266. doi:https://doi.org/10.1016/j.ijheatfluidflow.2016.09.015.

49. Termo Fluids S.L. \url{http://www.termofluids.com/}; ????

50. Balcázar N, Lehmkuhl O, Jofre L, Oliva A. Level-set simulations of buoyancy-driven motion of single and multiple bubbles. *International Journal of Heat and Fluid Flow* 2015;56:91–107. URL: http://www.sciencedirect.com/science/article/pii/S0142727X15000867. doi:http://dx.doi.org/10.1016/j.ijheatfluidflow.2015.07.004.

51. Balcázar N, Lehmkuhl O, Rigola J, Oliva A. A multiple marker level-set method for simulation of deformable fluid particles. *International Journal of Multiphase Flow* 2015;74:125–42. URL: http://www.sciencedirect.com/science/article/pii/S0301932215001019. doi:http://dx.doi.org/10.1016/j.ijmultiphaseflow.2015.04.009.

52. Balcázar N, Lehmkuhl O, Jofre L, Rigola J, Oliva A. A coupled volume-of-fluid/level-set method for simulation of two-phase flows on unstructured meshes. *Computers and Fluids* 2016;124:12–29.

53. Balcázar N, Castro J, Rigola J, Oliva A. DNS of the wall effect on the motion of bubble swarms. *Procedia Computer Science* 2017;108(Supplement C):2008–17. URL: http://www.sciencedirect.com/science/article/pii/S1877050917306142. doi:https://doi.org/10.1016/j.procs.2017.05.076.

54. Gutiérrez E, Favre F, Balcázar N, Amani A, Rigola J. Numerical approach to study bubbles and drops evolving through complex geometries by using a level set âĂŞ Moving mesh âĂŞ Immersed boundary method. *Chemical Engineering Journal* 2018;349(February):662–82. URL: https://doi.org/10.1016/j.cej.2018.05.110. doi:10.1016/j.cej.2018.05.110.

55. Amani A, Balcazar N, Naseri A, Oliva A. A Study on Binary Collision of GNF Droplets Using a Conservative Level-Set Method. In: *6th European Conference on Computational Mechanics (ECCM 6)- 7th European Conference on Computational Fluid Dynamics (ECFD 7)*. Glasgow, UK; 2018:.

56. Mason LR, Stevens GW, Harvie DJE. Multi-scale volume of fluid modelling of droplet coalescence. *The 9th International Conference on CFD in the Minerals and Process Industries* 2012;(December):1–6.

57. Jiang X, James AJ. Numerical simulation of the head-on collision of two equal-sized drops with van der Waals forces. *Journal of Engineering Mathematics* 2007;59(1):99–121. doi:10.1007/s10665-006-9091-9.

58. Willis K, Orme M. Binary droplet collisions in a vacuum environment: an experimental investigation of the role of viscosity. *Experiments in Fluids* 2003;34(1):28–41. URL: https://doi.org/10.1007/s00348-002-0526-4. doi:10.1007/

s00348-002-0526-4.

59. Focke C, Bothe D. Direct numerical simulation of binary off-center collisions of shear thinning droplets at high Weber numbers. *Physics of Fluids* 2012;24(7). URL: http://dx.doi.org/10.1063/1.4737582http://pof.aip.org/resource/1/PHFLE6/v24/i7http://pof.aip.org/http://pof.aip.org/about/about_the_journalhttp://pof.aip.org/features/most_downloadedhttp://pof.aip.org/authors. doi:10.1063/1.4737582.
60. Liu M, Bothe D. Numerical study of head-on droplet collisions at high Weber numbers. *Journal of Fluid Mechanics* 2016;789:785–805. doi:10.1017/jfm.2015.725.
61. Balcázar N, Rigola J, Castro J, Oliva A. A level-set model for thermocapillary motion of deformable fluid particles. *International Journal of Heat and Fluid Flow* 2016;0:1–20. URL: http://linkinghub.elsevier.com/retrieve/pii/S0142727X16301266. doi:10.1016/j.ijheatfluidflow.2016.09.015.
62. Gaskell PH, Lau AKC. Curvature???compensated convective transport: SMART, A new boundedness??? preserving transport algorithm. *International Journal for Numerical Methods in Fluids* 1988;8(6):617–41. doi:10.1002/fld.1650080602.
63. Sweby PK. High Resolution Schemes Using Flux Limiters for Hyperbolic Conservation Laws. *SIAM Journal on Numerical Analysis* 1984;21(5):995–1011. URL: http://epubs.siam.org/doi/10.1137/0721062. doi:10.1137/0721062.
64. Mashayek F, Ashgriz N. Nonlinear oscillations of drops with internal circulation. *Physics of Fluids* 1998;10(5):1071–82. doi:10.1063/1.869632.